Reactive halogens drive rapid mercury oxidation in hot volcanic emission-plumes

Alexander Nies[a,b,*], Jonas Kuhn[c,d], Bastien Geil[e], Jeroen Sonke[f], Nicole Bobrowski[g,d], Guillaume Dayma[h], Thorsten Hoffmann[e], Luke Surl[i], and Tjarda J. Roberts[b,a,*]

[*]Corresponding authors: alexander.nies0795@gmail.com (https://orcid.org/0009-0007-2039-0981), tjarda.roberts@lmd.ipsl.fr

[a] LPC2E, OSUC, Université d'Orléans, CNRS, CNES, 3. Avenue de la Recherche Scientifique, 45071 Orléans, France
[b] LMD/IPSL, ENS, Université PSL, École Polytechnique, Institute Polytechnique de Paris, Sorbonne Université, CNRS, 24 Rue Lhomond, 75231 Paris Cedex 05, France
[c] Department of Atmospheric and Oceanic Sciences, University of California, 520 Portola Plaza, 900095 Los Angeles, CA, USA
[d] Institute of Environmental Physics, Heidelberg University, Im Neuenheimer Feld 229, 69120 Heidelberg, Germany
[e] Department of Chemistry, University of Mainz, Duesbergweg 10-14, 55128 Mainz, Germany
[f] Géosciences Environnement Toulouse, CNRS/IRD/Université Paul Sabatier Toulouse 3, 14 Avenue Edouard Belin, 31400 Toulouse, France
[g] Istituto Nazionale di Geofisica e Vulcanologia, Osservatorio Etneo, Via Monti Rossi 12, 95030 Catania, Italy
[h] ICARE, University of Orléans, CNRS, 1C Avenue de la Recherche Scientifique, 45100 Orléans, France
[i] Department of Biosciences, University of Exeter, Stocker Road, EX4 4QD Exeter, United Kingdom

Preprint disclaimer

This manuscript is a non-peer-reviewed preprint submitted to EarthArXiv. It has also been submitted for consideration for publication in Earth and Planetary Science Letters (EPSL).

Abstract

Volcanoes release mercury (Hg) alongside gases and particles through continuous passive degassing and by explosive and effusive eruptions. The global dispersion and environmental impact depend on volcanic Hg oxidation state, which remains poorly constrained: thermochemical calculations of magmatic gas composition and crater-rim sampling indicate Hg to be predominantly in the reduced Hg^0 form that is relatively inert and disperses into the global atmosphere. However, several near-source plume observations report Hg^{II} forms that can be deposited locally and regionally, associated with important Hg^{II} uptake by volcanic ash. Oxidation of near-source volcanic plume Hg^0 into Hg^{II} is largely assumed to occur via photolytic atmospheric halogen chemistry. We tested this hypothesis in the fumarole field of Vulcano (Italy) by sampling Hg^0 and Hg^{II} at multiple distances from the fumarole source during day and night. Substantial (up to ~65%), near-source (< 50 cm, < ~1 s downwind) Hg^{II} detected during day and night rules out a significant role of photochemistry. Reanalysis of near-downwind (~minutes) ash-bound Hg datasets from explosive eruptions of Mt. Redoubt, Mt. Spurr, and Augustine volcano (Alaska, USA) supports fast oxidation during both day and night. Model simulations of chemical reactions in the hot, rapidly cooling volcanic plume identify high-temperature chemistry as a viable non-photolytic Hg oxidation mechanism that generates ~10% to ~80% Hg^{II}/Hg_{tot} within seconds following emission (but < 6% for halogen-poor emissions). Rapid high-temperature chemical processing therefore determines the oxidation state - and hence environmental fate - of volcanic Hg emissions into the atmosphere today and in the geological past.

Keywords:

volcanic mercury, mercury oxidation, mercury speciation, volcanic plumes, high-temperature chemistry

Highlights:

- Distance-resolved Hg^{II} measured in Vulcano fumarole plume during day and night.
- Hg present in deposits of volcanic ash from both day and night-time eruptions.
- Observed night-time Hg^{II} negates photolytic pathway for Hg^0 oxidation.
- High-temperature plume chemistry explains observed near-source Hg^{II}.

1 Introduction

Volcanoes are a natural source of atmospheric mercury (see e.g. (Edwards et al., 2021; Pyle and Mather, 2003)), yet total emissions and the oxidation state of volcanic mercury are poorly constrained. Mercury occurs mainly in two oxidation states in the atmosphere, as gaseous elemental mercury (GEM or Hg^0), or as oxidized mercury in oxidation state 2+ (Hg^{II}), which can be either in the gas-phase (gaseous oxidized mercury, GOM) or particle bound (PBM). Hg^0 is chemically relatively inert (lifetimes between 0.5 – 1 year, see e.g. (Horowitz et al., 2017)) and has a low water solubility and therefore is usually the main Hg species found in the background atmosphere. At volcanoes, thermodynamical equilibrium calculations suggest that the main mercury species in magmatic gases prior to emission into the atmosphere is Hg^0 (Aiuppa et al., 2007; Bagnato et al., 2007; Martin et al., 2011). However, oxidized Hg^{II} has been reported in several volcanic plumes, with fractions of total mercury as Hg^{II} ranging from only a few percent at the crater rims of Mt Etna (Italy), Telica and Masaya volcano (Nicaragua) (Bagnato et al., 2007; Witt et al., 2008), to up to 62% Hg^{II} reported in a previous study at Mt Etna summit craters (Dedeurwaerder et al., 1982). Low Hg^{II} is reported in the effusive eruption plume of Fagradalsfjall

(Iceland) (Edwards et al., 2024, 2023), whereas (Aiuppa et al., 2007) and (Zambardi et al., 2009) both found evidence for substantial oxidized Hg^{II} in fumarolic plumes at La Fossa crater on Vulcano island (Italy). Following explosive volcanic eruptions, formation of Hg^{II} is believed to drive mercury uptake onto ash, which can then gravitationally settle and deposit. Analysis of volcanic ash deposits by (Kushner et al., 2023) across three explosive volcano eruptions with distinct mercury contents (Mt. Redoubt 2009, Augustine volcano 2006, Mt. Spurr 1992) found that the downwind spatial variability was limited, concluding that mercury absorption to ash was driven by processes on sub-minute timescales following atmospheric injection. Collectively, these observations point to a rapid near-source formation of Hg^{II} in some volcanic plumes, although observations remain sparse. Quantifying mercury speciation and associated conversion pathways in volcanic plumes has been identified recently as one of the most important challenges in volcanic mercury research, since it has dramatic implications on overall flux estimations (Li et al., 2020), on Hg in the vicinity of the volcano (Edwards et al., 2021; Geyman et al., 2023), and on global Hg dispersion today and in the geological past (Zhou et al., 2024).

Mechanisms for conversion of volcanic Hg^0 into Hg^{II} are poorly understood. In aged volcanic plumes the atmospheric oxidation of the emitted SO_2 generates considerable sulfate particles, onto which mercury may be absorbed (Koenig et al., 2023). However, near-source volcanic plumes are likely too young for sufficient secondary sulfate formation to have occurred (Roberts et al., 2019). Volcanic emissions also contain halogens (HBr, HCl) which can be converted into reactive halogens such as BrO, OClO in the plume (e.g. (Bobrowski et al., 2007, 2003; Donovan et al., 2014; Roberts et al., 2014; Rüdiger et al., 2021; Surl et al., 2021; Von Glasow, 2010). Reactive halogens are known to be reactive to mercury and can convert Hg^0 into Hg^{II}. For example, oxidation of Hg^0 towards oxidized Hg^{II} by halogen species has been reported in the polar atmospheric boundary layer (Schroeder et al., 1998; Steffen et al., 2008; Wang et al., 2019), where the formation of reactive halogens is driven by a photolytic mechanism – the so-called 'bromine explosion' – that leads to mercury oxidation and mercury deposition events. A similar photolytic mechanism was proposed by (Von Glasow, 2010) to drive mercury oxidation in volcanic plumes. Furthermore, halogens also play an important role in the mitigation of Hg emissions from coal combustion powerplants (e.g. (Cao et al., 2008; Hughes et al., 2011; Niksa et al., 2010; Pavlish et al., 2003; Preciado et al., 2014; Yang et al., 2017)), where halogen activation and the Hg^0 transformation into Hg^{II} is driven by high-temperature chemistry. The relevance of similar high-temperature mercury oxidation mechanisms in volcanic plumes is investigated in this study.

Our current understanding of mercury oxidation in volcanic plumes is subject to observational and modeling limitations:

(1) Studies of mercury in the near-source volcanic plume typically rely on individual point measurements, without resolving temporal trends in mercury oxidation. There is for instance a lack of simultaneous measurements of speciated mercury over distance downwind and systematic studies distinguishing between day and night to assess the influence of solar radiation on mercury oxidation.

(2) Oxidation of mercury in volcanic plumes is typically assumed to be associated with reactive halogen chemistry, specifically during the photolytic formation of BrO in the downwind plume (e.g. Von Glasow, 2010). A complete process-based understanding of Hg transformations in near-source volcanic plumes also requires considering high-temperature chemistry of the hot gas plumes shortly after emission.

(3) Most prior studies of the early, high-temperature plume environment relied on thermochemical equilibrium modeling (e.g. (Gerlach, 2004; Martin et al., 2011, 2006).

However, it has been shown that the chemistry at the interface between magma (or hot magmatic gases) and the atmosphere is determined by chemical kinetics (Kuhn et al., 2022; Roberts et al., 2019). Kinetics-based simulations of the chemistry of the rapidly diluting and cooling plume can contribute significantly to a better understanding of high-temperature emission processes and resulting cooled plume composition (Nies et al., 2025). This work seeks to quantify Hg speciation and elucidate central pathways for mercury oxidation in the near-source plume. We conducted day and night-time measurements of speciated mercury (Hg^0 and Hg^{II}) with co-measured SO_2 at different distances from a fumarolic source at La Fossa crater, Vulcano in 2019 and 2023. Diurnal influences were additionally assessed using a dataset of near-downwind ash-bound mercury from explosive eruptions (Kushner et al., 2023). To interpret the observations we incorporated high-temperature mercury reactions interacting with C-H-O-S-Br-Cl in a kinetic model (Nies et al., 2025) that simulates plume chemical transformations during the critical first seconds when the hot gas emission mixes with the cool oxidizing atmosphere.

2 Methods

We conducted a field-campaign at La Fossa crater fumarole field on Vulcano in September 2019 and September 2023. The sampling strategy aimed at undertaking simultaneous measurements of mercury speciation during day and night and at different distances from the emission sources (Figure 1 A, B), resulting in 25 valid samples (simultaneous results for Hg^0 and Hg^{II}, 17 during daytime and 8 during night) from both campaigns. In 2023, co-measurements of SO_2 by an electrochemical sensor quantified sample-specific plume exposure for 19 of the mercury samples. We performed four experiments (including one at night) with distance-resolved simultaneous measurements at fumarole F0 (up to 4 distance points in the downwind plume). Full analytical results of the measurements are given in Table S 1 and Figure S 1, including tests for statistical robustness and breakthrough tests.

2.1 Filter based sampling of speciated Hg in Vulcano fumaroles

Mercury samples were taken by a staged filter setup, with an initial stage consisting of Polyethersulfone (PES) membranes to capture oxidized Hg^{II} (GOM and PBM), followed by an activated carbon trap (HGR-AC) to capture Hg^0. Up to four Hg sampling trains were simultaneously deployed (see e.g. Figure 1 A and B). Volcanic gases are pumped through the filters with KNF and GilAir pumps at a volume flux of 1 L/min. (Edwards et al., 2023) shows that integrated Hg^0 activated carbon trap measurements are similar to well established sampling techniques like time averaged samples with Lumex instruments and passive air collection, but it is less prone to H_2S interferences which can inhibit adsorption of mercury onto gold traps (Ferrara et al., 2000; Schroeder et al., 1995).

The PES membranes were acid leached in the laboratory in 10 mL of 2.5% v/v concentrated bi-distilled HNO_3/HCl in a 2:1 ratio in acid cleaned 50 mL PFA Teflon beakers (Savillex) on a heated plate (Analab) for 12 h at 120 °C. The Hg^{II} concentration in the leachates was determined using a Brooks Rand Model III CV-AFS with a custom made purge and trap system (Heimbürger et al., 2015). The CV-AFS was calibrated using the NIST 3133 Hg standard reference material and independently validated against the ERM-CA400 standard with good results of 17.5 ± 1.3 ng/L measured and 16.8 ± 0.3 ng/L certified. The CV-AFS limit of detection (LOD) was 5 pg Hg, and the PES filter field blanks contained 83 ± 38 pg Hg with an associated field LOD of 197 pg Hg^{II}. Five out of 30 PES samples in the 2023 campaign were below the field LOD.

The HGR-AC traps were combusted at 900 °C for 3 h in a double-stage tube furnace in air at 80 mL/min, and purged and pre-concentrated into 5 mL of 40% v/v HNO_3/HCl in a ratio of 2:1 (Sun et al., 2013). Purging impingers were rinsed with a total volume of 5 mL of MilliQ water, diluting the sample to 20% v/v acid. The final trapping solutions were kept in a refrigerator at 4 °C until mercury analysis. The certified reference material NIST 1632D (coal, n=8) was processed along with the samples. Mercury concentrations were analyzed by CV-AFS as described above. Field AC blanks contained 0.13 ± 0.10 ng of Hg, and 3 out of 28 samples were below the field LOD of 0.45 ng Hg.

2.2 Co-measurements of SO_2

Electrochemical sensors for SO_2 sampling were co-deployed next to the Hg sampling trains to determine in-situ plume exposure during sampling and calculate the Hg/SO_2 ratio, where SO_2 serves as a quasi-inert dilution tracer for volcanic gases on seconds times-scales at Vulcano (Aiuppa et al., 2007). Electrochemical sensors are manufactured by Alphasense (UK) and are directly exposed to volcanic gases in a self-build apparatus. The sensor heads are mounted in 3D printed houses connected to a box which includes batteries and a HOBO datalogger. Data is collected with a frequency of 1 Hz. Sensors were calibrated by the manufacturer shortly prior to deployment. Sensor signals are response-time corrected (Karbach et al., 2022) and time averaged over the Hg sampling period (see Figure S 2 for an exemplary dataset and Table S 1 for the results). The mixing ratio is then converted into a mass concentration according to ambient pressure (P = 1013 hPa) and temperature (T = 300 K). The statistical error on the average is negligible compared to the error introduced by calibration of the sensors. This error is estimated to be a maximum of 10% of the signal according to inter-comparison of the sensors during the field measurements (see Figure S 3).

2.3 High-temperature plume chemistry model

Measurements are interpreted by using a high-temperature plume chemistry model, that simulates chemical kinetics alongside a mixing and dilution trajectory (Kuhn et al., 2022; Nies et al., 2025). The underlying reaction rate constants and their temperature dependencies are based on laboratory experiments and includes C-H-O-N-S chemistry and sub-mechanisms for halogens (Cl and Br) and Hg (Bedjanian, 2022, 2022, 2021; Hughes et al., 2011; Niksa et al., 2010; Zeng et al., 2021). The model requires emission temperature and gas composition as key initialization inputs. For the fumarolic field at La Fossa crater on Vulcano island, gas composition for the major volatiles have been estimated for fumarole F0 (Aiuppa et al., 2007) which was the main focus of the measurement campaign. Bromine emissions were obtained through alkaline trap measurements (Wittmer et al., 2014) during the 2023 campaign, yielding a corresponding Br/Cl molar ratio of 4.4×10^{-4}. Total mercury emissions are obtained from its respective ratio to SO_2 (see Figure 1) from the campaign measurements. Halogen and mercury species are emitted in their reduced forms HCl, HBr and Hg^0 respectively, reflecting magmatic equilibrium. Emission temperatures for Vulcano fumaroles have previously been estimated at 560 K (F0) (Aiuppa et al., 2007). We applied the 560 K F0 temperature, which closely matches the temperature measurement of 581 K in September 2023 by (Paonita et al., 2025) and investigated the influence of up to ± 200 K warmer or cooler emission temperatures on the chemistry in the near source fumarolic plume. This temperature range falls well within the temperature variability observed in long-term datasets of Vulcano fumaroles (see e.g. (Paonita et al., 2025)). We also performed sensitivity tests, in which we varied the rate of mixing of air and magmatic gases by a factor of 100 compared to the base run. To provide wider

insights to volcanic plume mercury chemistry beyond Vulcano, we investigated two contrasting cases: Mt. Redoubt 2009 (Alaska USA), a series of halogen-rich explosive eruptions where ash-bound mercury is reported, (Kushner et al., 2023), which we reanalyzed in terms of eruption timing (day or night). The second study is at Fagradalsfjall 2021-2022 (Iceland), a halogen-poor effusive emission plume where speciated mercury is reported (Edwards et al., 2024, 2023). For the 2009 Mt. Redoubt eruptions, gas emission temperatures are estimated to be in the range of 998–1273 K (Werner et al., 2013). The model gas composition is based on measurements of an eruptive episode in 2010 (Kelly et al., 2013; Werner et al., 2013) and a Hg/SO_2 mass ratio of 1×10^{-5} is applied to be similar to other North American volcanoes (e.g. $0.5 \times 10^{-6} < Hg/SO_2 < 1 \times 10^{-3}$ Mt St. Helens, Mt. Shasta, Mt. Hood (Edwards et al., 2021)). For the halogen-poor Fagradalsfjall plume, gas emission compositions are based on (Scott et al., 2023) and $Hg/SO_2 = 1.8 \times 10^{-8}$ from (Edwards et al., 2023), with an emission temperature 1473 K (Scott et al., 2023), and sensitivity tests at 200 K and 400 K lower. The model initializations and a detailed description of calculations involved to provide full compositions are summarized in Table S 2. Physical parameters of the model runs are shown in Figure S 4.

3 Results and Discussion

3.1 Vulcano is a stable Hg source

Our field-observations confirm that Vulcano fumaroles are a strong local source of mercury with a mass ratio of total mercury ($Hg_{tot} = Hg^0 + Hg^{II}$) to SO_2 of $(5.3 \pm 1.0) \times 10^{-7}$ (see Figure 1). This Hg_{tot}/SO_2 mass ratio is similar to previous estimates (Aiuppa et al., 2007; Bichler et al., 1995; Di Liberto et al., 2002; Edner et al., 1994; Ferrara et al., 2000; Zambardi et al., 2009). The Hg_{tot}/SO_2 mass ratios are broadly constant within an order of magnitude, even though our 2023 study falls into a Vulcano degassing crisis (see e.g. (Neri et al., 2025)). The measurements for this work are mainly performed at fumarole F0, except for two data points from F8/9 (see Figure S 1) and are all near-source plume samples (distances between 0.5 m and up to 15 m) in contrast to fumarole samples taken directly inside the fumarole gas outlet in some prior studies. Furthermore, Figure S 1 D confirms that no biases in the Hg_{tot}/SO_2 ratio with SO_2 concentration across the dataset.

3.2 Day and night study reveals that near-source Hg oxidation is non-photolytic

Our field-study investigated mercury speciation (Hg^0 and Hg^{II}) during day and night and at different distances from source. Figure 1 A shows an example image from the 2023 sampling at fumarole F0 during sunset. The picture illustrates the at-source sampling point with measurement devices placed as close to the fumarole emission as possible. Panel B shows a typical sampling setup with three different measurement stations placed at different distances in the fumarolic plume. Analysis of the ratio between Hg^{II}/Hg_{tot} between the day and night samples finds that there are no significant statistical differences (two-sample t-test: $t = -0.54$, $p = 0.60$) between these two groups (see Figure 2 A). This finding rules out any significant influence by photochemistry on the oxidation of Hg in the Vulcano fumarolic plumes. Near-downwind formation of Hg^{II} has also been inferred from analysis of mercury in volcanic ash deposits from three eruptions in Alaska (Kushner et al., 2023), who concluded that the mercury oxidation and adsorption to ash must occur on sub-minute timescales. In Figure 2 B we present the reported ash deposit data, here sorted by eruption time (day, night or mixed being samples of explosions both during day and night (Miller et al., 1998; Wallace et al., 2010, 2013)). Each individual eruption has a distinct mercury signature (see (Kushner et al., 2023)) but we find no statistically significant variation in mercury abundance between day and night, including for the Mt. Redoubt eruption that has the most data points. A

distance resolved analysis of the complete dataset is shown in the Supplement (Figure S 5), with no evidence for any trend in mercury oxidation related to eruption time and distance for the individual volcanoes. The observations from Vulcano supported by reanalysis of (Kushner et al., 2023) provide evidence that the oxidation of Hg^0 into Hg^{II} occurred via non-photolytic processes.

3.3 High at-source abundances of Hg^{II} evidence very fast oxidation of volcanic Hg emissions

According to thermochemical equilibrium models (Aiuppa et al., 2007; Bagnato et al., 2007). mercury in magmatic gases is predicted to occur predominantly as Hg^0, in contrast to our fumarolic plume measurements of Hg^{II} at Vulcano. To provide further insight, our distance-resolved plume observations are presented in two categories (at-source emission and downwind plume, Figure 3 A). At-source samples are taken as close as possible to the visible fumarole outlet, which is always closer than 50 cm from the visible fumarole outlet. Plume samples are taken at a distance from the emission source of several meters (more than 5 m and up to 15 m). Samples are again categorized as day and nighttime. We find high at-source abundances of Hg^{II} with up to 65% of total Hg being oxidized within 50 cm (below 1 s of plume age) from the emission source. Furthermore, there is no evidence for additional oxidation downwind with a large range of Hg^{II} in the plume observations between 10% and 80%. The high at-source abundance of Hg^{II}, together with the absence of further downwind oxidation, contrasts with previous observations suggesting progressive in-plume processing of Hg, including oxidation and partitioning of Hg^0 into particulate Hg^{II} with increasing plume age (Aiuppa et al., 2007; Zambardi et al., 2009). There is no trend in mercury speciation with sampling time (equivalently sampling volume) and plume exposure (see Figure S 1 B and C), ruling out obvious sampling artefacts as an explanation for the observed speciation pattern.

3.4 High-temperature formation of HO_x and reactive halogens drive rapid Hg^0 oxidation

Our field-observations at Vulcano and analysis of ash deposits (particularly from Mt. Redoubt, (Kushner et al., 2023)) evidence that Hg^{II} is rapidly formed in these volcanic plumes during both day and night. Thus, mercury in these near-source plumes cannot be oxidized by reactive halogens formed via a photochemical pathway (Von Glasow, 2010). A plausible non-photlytic mechanism to oxidize mercury can be the activation of halogens via high-temperature chemistry. In the following we apply our recently developed kinetics-based model that simulates high-temperature chemical reactions in a rapidly dispersing and cooling volcanic plume (Nies et al., 2025). Our model traces high-temperature chemistry while continuous turbulent entrainment of air cools the emitted gas within sub-seconds to seconds (see Figure 3 B and Figure S 4 A-I). Within the initially hot gas mixture H_2O-rich magmatic gases and O_2-rich air create a transient, highly oxidizing environment, which strongly influences the chemistry and composition of the cooled plume (Kuhn et al., 2022; Nies et al., 2025; Roberts et al., 2019).

Figure 3 B-E shows the results of a typical model run for Vulcano focused on the species relevant for the gas-phase oxidation of mercury. Panel B shows that the plume cools in less than 10 s from the emission temperature of magmatic gases down to atmospheric temperatures. The model simulates the full suite of gas-phase oxidation reactions of mercury in high-temperature volcanic emissions, which is a three-step process. The first step is the formation of HO_x radicals at the interface between magmatic gases and the atmosphere. In-mixed O_2 reacts with hot water vapor from the volcanic emissions and rapidly forms OH and HO_2 concentrations exceeding the atmospheric background by many orders of magnitude (Figure 3 C). This process occurs via a chain reaction that is highly temperature dependent (see e.g. (Kuhn et al., 2022; Nies et al., 2025;

Roberts et al., 2019)). In the second step, the HO_x radicals react with hydrogen halides (HBr and HCl) to form reactive halogen species such as Br, Cl, BrCl, Br_2, and Cl_2 ((Nies et al., 2025), Figure 3 D). In the third step, these reactive halogen species react with Hg^0 and form Hg^{II} in the form of $HgBr_2$, $HgCl_2$, and HgBrCl (Figure 3 E). Direct oxidation of Hg by OH forming HgOH (Hg species in oxidation state +1), which can be further oxidized to Hg^{II} in the normal background atmosphere (Saiz-Lopez et al., 2022), is not a relevant process despite the high initial abundances of OH, because HgOH is destroyed thermochemically very fast.

Conversion of Hg^0 into Hg^{II} in volcanic plumes depends non-linearly on temperature and emission composition, as shown by three case studies (Vulcano fumarole, Mt. Redoubt and Fagradalsfjall plume, Figure 4). Greater Hg^{II}/Hg_{tot} is formed in plumes with higher emission temperatures, and for halogen-rich emissions (Vulcano, Mt. Redoubt) than for halogen-poor Fagradalsfjall.

In the Vulcano case, the simulation at T_0 = 560 K (F0 temperature estimate, (Aiuppa et al., 2007)) produces around 15% Hg^{II} after 3 s (see Figure S 6), whilst an emission temperature +100 K higher (as has been reported for Vulcano fumaroles, e.g. (Giggenbach et al., 2001; Paonita et al., 2025)) yields 90% Hg^{II} after 5 s. This range is broadly consistent with our observed Hg^{II}/Hg_{tot} ratio magnitudes at Vulcano (see Figure 2 A, Figure 4). In contrast, for emission temperatures far below the typical fumarole outlet temperature (T_0 = 360, 460 K), model simulations yield very low Hg^{II} abundances and gas-phase oxidation of Hg becomes negligible. Simulated Vulcano Hg^{II} speciation is dominated by $HgCl_2$ and HgBrCl due to the high abundances of reactive chlorine species (Figure 3 E). This originates from a relatively high chlorine/sulfur ratio in the emission in combination with a low bromine/chlorine ratio (Table S 2). Plume chemistry generates Cl radicals that can efficiently oxidize Hg^0 to oxidation state +1 (Hg^I) intermediates at relatively low temperatures. This is facilitated by the inverse temperature dependence (negative activation energy) of the $Hg^0 + Cl + M$ reaction, which is the main pathway for forming Hg^I intermediates. These species can subsequently be oxidized by Cl_2, the dominant reactive chlorine species in the F0 Vulcano simulation, to form $HgCl_2$.

For Redoubt plume, the modeled formation of Hg^{II} is consistent with the conclusions from (Kushner et al., 2023) that mercury oxidation occurred on short near-downwind (sub-minute) scales (Figure 4, Figure S 6). Our two simulations cover the range in emission temperatures for the Mt Redoubt eruptions (Werner et al., 2013). As expected, the high emission temperature run (T_0 = 1273 K) shows greater Hg^{II} formation up to 90% within 10 s (see Figure S 6), with the lower temperature run (T_0 = 923 K) yielding 18% Hg^{II}. In Redoubt plume, the main Hg^{II} species are HgBrCl and $HgBr_2$ (Figure S 7), which is due to the higher emission temperatures and the higher Br/S ratio in the emission (Table S 2). The dominant reactive halogen species in the plume is reactive bromine (Br, Br_2, and BrCl, Figure S 8). Additionally, higher HO_x abundances driven by higher temperatures can lead to back reactions of Hg^{II} species to Hg^I and Hg^0 via H or OH radicals. These distinctions lead to comparable modeled Hg^{II} formation at Mt Redoubt and Vulcano, despite their contrasting emission temperatures.

For the Fagradalsfjall effusive eruption plume (Figure 4), model simulations yield very low Hg^{II} abundances (< 6%) for all scenarios, despite the high emission temperatures (T_0 = 1473, 1273, 1073 K). This is due to the much lower halogen content of Fagradalsfjall emissions compared to Redoubt (or Vulcano). The approximately one order of magnitude lower halogen to sulfur ratio (Table S 2) limits high-temperature halogen-mediated oxidation of Hg in the Fagradalsfjall plume. Our modeled low Hg^{II}/Hg_{tot} ratio (few percent) is consistent with UAV-based measurements of mercury speciation (Edwards et al., 2024) which report near-source plume mercury dominated by Hg^0 in the Fagradalsfjall plume.

Our model simulations predict greater Hg^{II} for high emission temperatures and high halogen abundances with a dependence on the speciation of halogen radicals available (Figure 4). Plume temperature and chemistry can also be affected by the dilution (cooling) rate. Sensitivity tests undertaken across a wide-range of mixing scenarios (×100 slower/faster in-mixing of air compared to base run, see Supplement in Figure S 9, Figure S 10 and Figure S 11) confirm that substantial Hg^{II} is formed in halogen-rich emission-plumes (Vulcano and Mt. Redoubt) with limited Hg^{II} in halogen-poor Fagradalsfjall. Generally, slower mixing scenarios allow more time at high temperatures where mercury oxidation reactions proceed compared to faster mixing scenarios that cool quicker, although the chemistry is non-linear. At Vulcano, our field-observations at fumarole F0 suggest that Hg^{II} formation may occur on even shorter timescales than our base-run model simulations (few seconds), which also underestimate Hg^{II}/Hg_{tot}, assuming T_0 = 560 K (but not for T_0 = 660 K). Aside from the inherent uncertainty in emission temperatures or in rate constant temperature dependencies, a possible explanation includes air-entrainment into the porous subsurface, enabling some chemistry (slow mixing) prior to outlet release. It is also possible that high-temperature gas-phase halogen activation may trigger additional heterogeneous (gas-aerosol) halogen processes that can enhance the proportion of mercury oxidized, as has been suggested to occur on metal-rich fly-ash in coal power stations (Yang et al., 2020).

3.5 Decreasing Hg^{II} in the first seconds of cooled concentrated plumes

Our Vulcano fumarole field-measurements showed that Hg^{II} is formed extremely close to source, with no evidence for further in-plume oxidation of Hg^0 beyond 0.5 m downwind (Figure 3 A). Furthermore, four field-experiments conducted simultaneous speciated mercury sampling at different distances downwind (up to 15 m) and identified evidence for decreasing Hg^{II} in the plume: Figure 5 shows the Hg^{II}/Hg_{tot} ratio against distance for the four distance-resolved experiments during the 2023 campaign at fumarole F0. Each experiment (3 during daytime, 1 during night) shows a decreasing trend with distance or equivalently plume age, yielding overall e-folding lifetimes of Hg^{II} between 7 and 44 s under the assumption of ground windspeeds between 0.5 and 3 m/s (see Figure S 12 and Figure S 13 for different windspeed assumptions). This corresponds to an e-folding distance of around 20 m from source. One possible cause of the observed Hg^{II} loss is deposition onto local ground-rock. Three out of the four experiments show an overall decrease in Hg_{tot}/SO_2 between the at-source measurements and the far downwind samples (15 m), with strongest decrease in the first 7 m (see Figure S 14 A). This pattern could be explained by the deposition of Hg^{II} to surfaces, thereby decreasing Hg^{II}/Hg_{tot} and Hg_{tot}/SO_2, whilst Hg^0/SO_2 remains largely constant, indicating chemical inertness in the cooled, dispersing plume (see Figure S 14 B, C). Alternatively, we note that, following mercury oxidation, some Hg^{II} reduction and Hg^0 re-emission has also been reported across stack environments at coal power stations (e.g. (Chang et al., 2017, 2017; Hsu et al., 2021; Krzyżyńska et al., 2020; Solis et al., 2017)). The Hg^{II} reduction is believed to be caused by fluid phase chemistry in the slurry of wet scrubbers installed to capture sulfur species in the flue gases, as a complex function of pH, sulfite concentration, dissolved oxygen, halogen concentrations and gas-liquid mass-transfer (see e.g. (Solis et al., 2017)). Future work should consider whether a similar reduction mechanism could proceed in the highly concentrated near-source volcanic plumes. Deposition of Hg^{II} on the crater wall or chemical reduction pathways may impact measurements of speciated mercury at the volcano crater rim (i.e. plume age of tens of seconds up to minutes), at volcanoes such as Masaya (Witt et al., 2008), and particularly Mt. Etna, where reported observations of Hg^{II} are highly variable (Bagnato et al., 2007; Dedeurwaerder et al., 1982).

4 Conclusions

This study investigated whether near-source volcanic mercury speciation is controlled primarily by thermodynamic equilibrium during magmatic degassing, photochemical plume processing, or rapid high-temperature plume chemistry. We find that Hg oxidation occurs during day and night, with Hg^{II} observed during the earliest stages of fumarolic plume cooling and mixing at Vulcano. Reanalysis of ash deposits from explosive eruptions, including Mt. Redoubt, provides independent evidence for sub-minute Hg oxidation and ash-bound mercury under both daytime and nighttime conditions (Kushner et al., 2023).

The observed Hg^{II} abundances cannot be explained by equilibrium thermodynamics, and presence of Hg^{II} at night rules out a photochemical mechanism as a primary mechanism for near-source mercury oxidation. Instead, the observations indicate high-temperature kinetic processes operating close to the emission source. Kinetic model simulations show that rapid high-temperature reactions can convert Hg^0 to Hg^{II} under halogen-rich emission conditions, through reactions with reactive halogens formed in the early high-temperature plume, consistent with field observations at halogen-rich Vulcano fumaroles and Mt. Redoubt ash deposits (Kushner et al., 2023) and with low Hg^{II} abundances in the halogen-poor Fagradalsfjall plume (Edwards et al., 2024). Our Vulcano observations also suggest subsequent Hg^{II} loss, potentially through deposition onto nearby rock surfaces. Taken together, our observations and modelling demonstrate that rapid near-source Hg oxidation in volcanic plumes is governed by the interplay between high-temperature chemistry and halogen availability.

The modeled sensitivity of Hg^{II} formation to emission temperature, gas composition, and plume mixing highlights the strongly non-linear nature of volcanic mercury chemistry. This sensitivity is especially important because vent temperatures and near-vent mixing processes remain imperfectly constrained in many volcanic systems. Further uncertainties arise from the limited constraints on kinetic reaction rates under the rapidly changing temperature and chemical conditions of the near-source plume, particularly for reactions involving H_2S (see e.g. (Colom-Díaz et al., 2021; Nies et al., 2025; Raj et al., 2020). Multiphase reactions on aerosols may also contribute alongside the gas-phase chemistry simulated here.

The multiphase bromine explosion chemistry that develops in dilute volcanic plumes (Surl et al., 2021; Von Glasow, 2010) requires photochemistry and therefore cannot explain the near-source Hg^{II} observed here, which we attribute to rapid high-temperature reactions. Nevertheless, mercury oxidation associated with photochemical formation of reactive halogens may become important at older plume ages and regional scales. (Koenig et al., 2023) reports day and night-time oxidation of mercury in the ~4 h aged plume of Piton de la Fournaise (Reunion Island, France) which cannot be explained by high-temperature chemistry. They observe complete Hg^0 depletion in the aged volcanic plume, which may reflect mercury uptake to abundant secondary sulfate particles formed during plume evolution. However, observations remain too limited to establish the role of heterogeneous processes in volcanic mercury redox chemistry.

Our observations and model findings demonstrate that volcanic mercury emissions should be treated as spatially and temporally evolving chemical systems rather than fixed source compositions defined by equilibrium degassing alone. This complexity has broad implications for volcanic mercury emission estimates and environmental impact assessments. Many volcanic mercury flux calculations rely on Hg^0/SO_2 ratios measured in cooled or distal plumes and implicitly assume that emitted mercury remains predominantly in elemental form (Li et al., 2020; Pyle and Mather, 2003), or use estimates of mercury speciation (e.g., (Edwards et al., 2021)).

Given the large variability in Hg^{II} abundances and the complex redox chemistry of mercury, such approaches may underestimate the contribution of oxidized Hg to volcanic emissions where rapid near-source Hg^{II} formation occurs, particularly under halogen-rich and sufficiently hot emission conditions. Large-scale assessments of the global impacts of volcanic mercury strongly depend on assumed source speciation (Geyman et al., 2023; Li et al., 2020), but generally do not resolve the near-source processes that transform Hg^0 into Hg^{II}.

Future work should focus on identifying and constraining the kinetics of heterogeneous mercury oxidation pathways in volcanic plumes, including the roles of sunlight, sulfate, and halogen-bearing particles across different emission temperatures and mixing-cooling regimes. Extending speciated mercury measurements and kinetic modelling to a wider range of volcanic systems will help determine how broadly the rapid near-source redox chemistry identified here applies across different gas compositions and eruptive styles. Together, these approaches are essential for establishing how high-temperature halogen chemistry, photochemical processing, and heterogeneous reactions collectively control the evolution of volcanic mercury in the atmosphere.

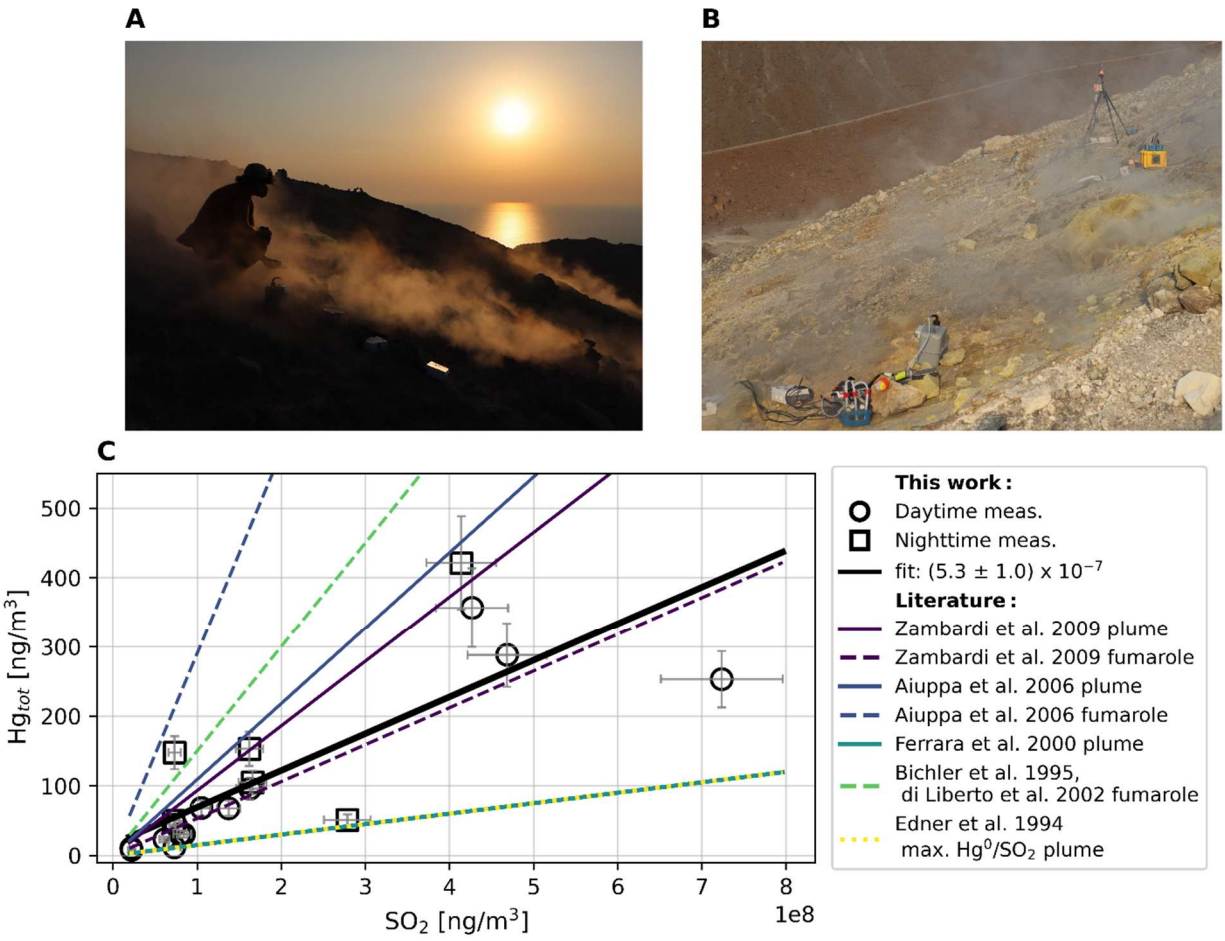

Figure 1: Field sampling conditions and Hg_{tot}/SO_2 ratio in Vulcano fumaroles

Panel A: Picture of the sampling conditions during sunset between the day and nighttime period. Panel B: Typical sampling setup for simultaneous measurements at three different distances. Panel C: Scatterplot of total Hg mass (Hg_{tot}) against SO_2 mass concentration measured during the Vulcano field campaign. SO_2 mixing ratio is measured alongside Hg sampling and converted into average mass concentration according to ambient pressure and temperature. The statistical error of the SO_2 measurement is on the order of the size of the marker, thus the dominant error source is assumed to be the calibration of the sensor itself estimated to be 10%. The black line shows a linear regression yielding a Hg_{tot}/SO_2 ratio of $(5.3\pm1.0)\times10^{-7}+(16\pm25)$ with a correlation coefficient of $R^2 = 0.64$. The colored lines correspond to earlier measurements of Hg speciation in Vulcano fumaroles (Aiuppa et al., 2007; Bichler et al., 1995; Di Liberto et al., 2002; Edner et al., 1994; Ferrara et al., 2000; Zambardi et al., 2009). Plume samples (solid lines) are taken at a distance to the emission source by various filter setups, while fumarole samples (dashed lines) are taken directly inside the emission source by inserting tubes into the fumarole avoiding interaction with atmospheric air prior to sampling.

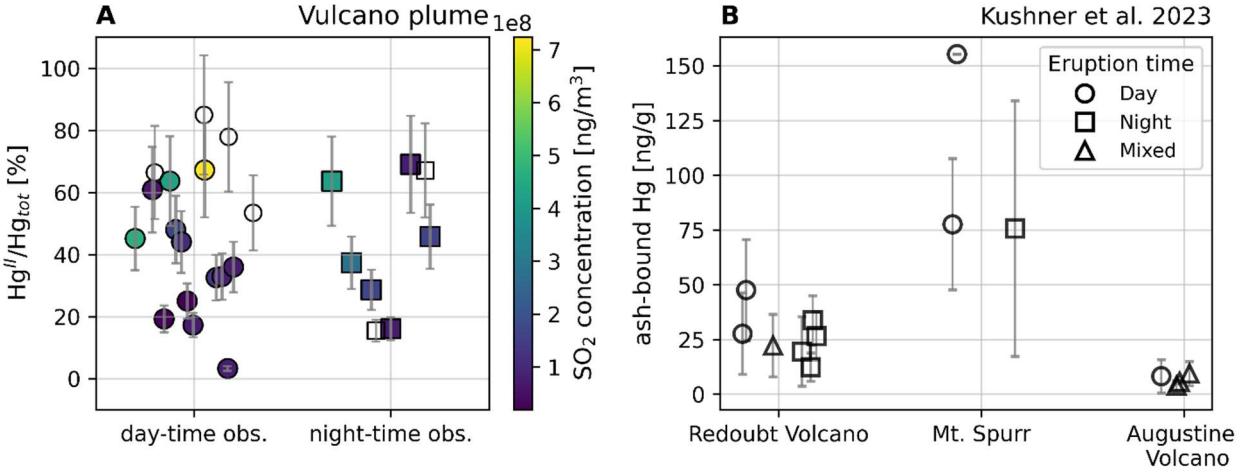

Figure 2: Day–night invariance of volcanic Hg speciation at Vulcano and in ash-bound Hg from Alaskan volcanoes

Comparison of day- and nighttime observations of Hg^{II}/Hg_{tot} at Vulcano and ash-bound mercury at Redoubt. Panel A: Hg^{II}/Hg_{tot} ratio in % separated in day (round markers) and night-time samples (squared markers) from the 2019 and 2023 field campaigns in the Vulcano fumarolic plume. Color coded are the SO_2 concentrations co-measured as indicated in Panel A and B from Figure 1. Colorless markers indicate measurements from the 2019 campaign without co-measured SO_2. Day and night samples show no statistical difference in the Hg^{II}/Hg_{tot} ratio. Panel B: Ash-bound Hg concentrations from three Alaskan volcanoes with distinct mercury emissions, showing mean and standard deviation in mercury per g ash for the eruption events reported by (Kushner et al., 2023). Here, eruption events are furthermore categorized with the different markers showing if the eruption took place during day or night. Mixed eruptions are either spanning day, and nighttime or eruption times could not be determined certainly.

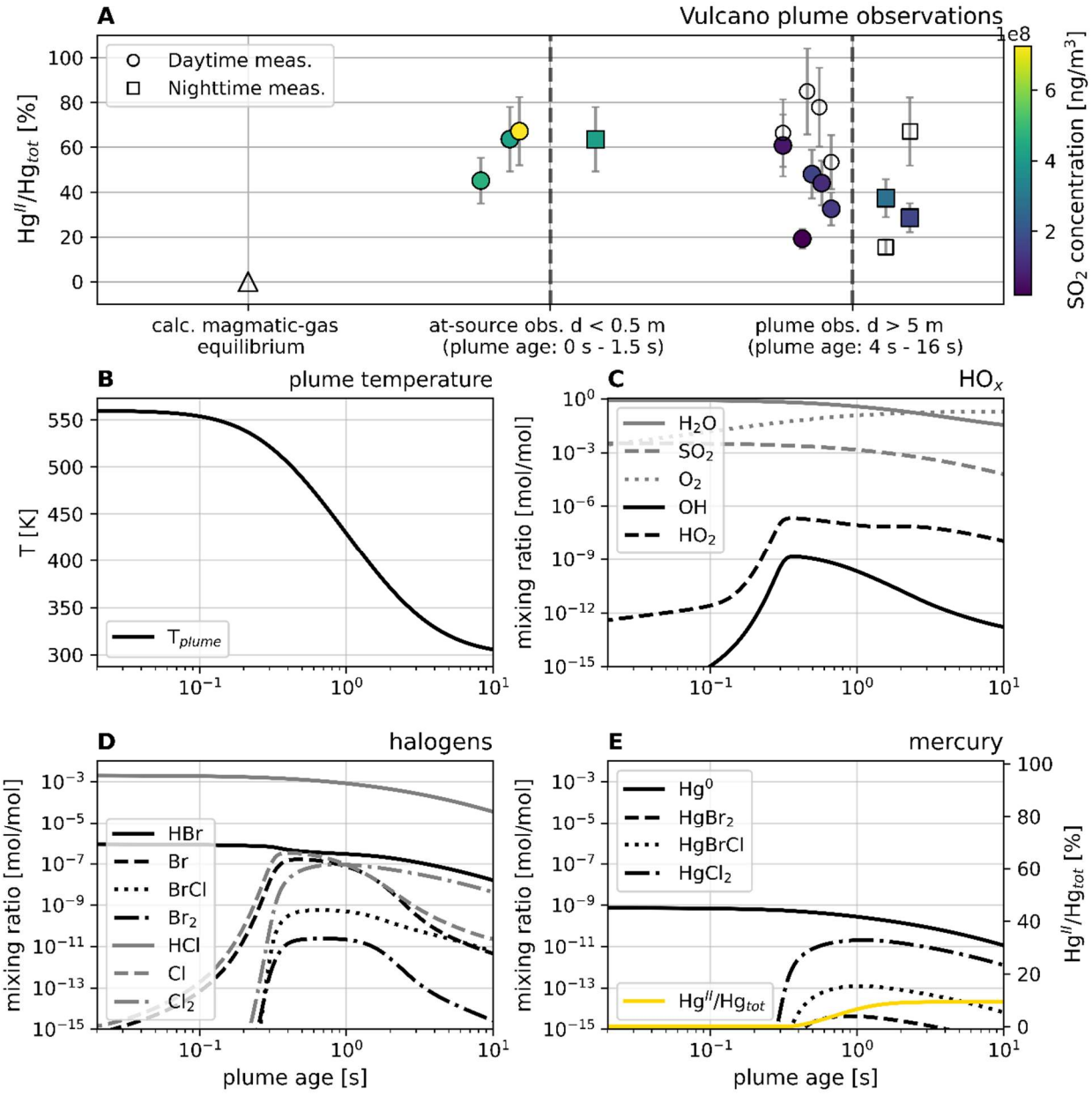

Figure 3: Observed and modelled Hg speciation during early-stage plume evolution

Panel A: Plume mercury speciation from the 2023 measurement campaign compared to Hg speciation in the pure volcanic gases (prior to interaction with atmospheric air) calculated from thermochemical equilibrium (Aiuppa et al., 2007; Bagnato et al., 2007). Measurements are categorized by distance, with at-source measurements as close as possible to the visible fumarole outlet (distance < 50 cm and plume age below 1.5 s) and plume observations more than 5 m downwind and plume ages between 4 s and 16 s. The plume ages are inferred, assuming a wind speed between 0.5 m/s and up to 3 m/s. Panels B to E show typical simulation results for an F0 fumarolic composition. Panel B: Plume temperature evolution, with a cooling trajectory from the emission temperature of 560 K down to surrounding temperatures of 300 K within 10 s. Panel C: Evolution of the two main HO_x radicals (OH and HO_2) formed by high-temperature chemistry. H_2O and SO_2 are shown as dilution tracers as well as the amount of in-mixed O_2. Panel D: Main reactive halogen species involved in the oxidation of Hg and that are formed by HO_x-driven oxidation of the emitted hydrogen halides (HCl and HBr). Panel E: Formation of gaseous reactive Hg^{II} species from

emitted Hg^0 as well as the Hg^{II}/Hg_{tot} ratio in [%] on the second y-axis, a parameter observed during the Vulcano field campaigns.

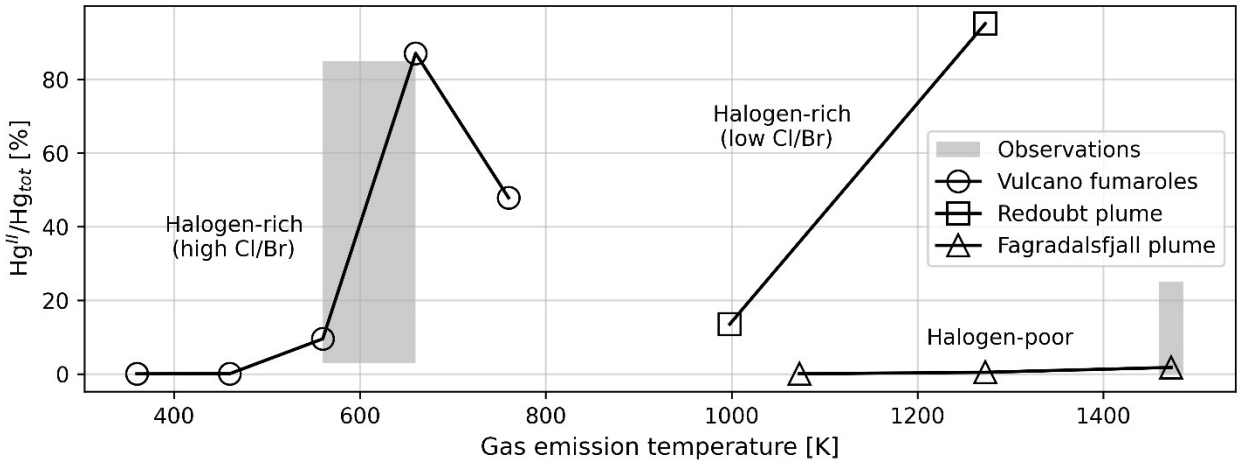

Figure 4: Temperature sensitivity of Hg oxidation across contrasting volcanic gas compositions

Hg^{II}/Hg_{tot} model sensitivity study for three cases with distinct gas compositions (halogen-rich Vulcano, Redoubt and halogen-poor Fagradalsfjall). Plotted is the final Hg^{II}/Hg_{tot} ratio in % against the gas emission temperature which is varied as a sensitivity test for the individual simulation. The shaded region shows the observed Hg^{II}/Hg_{tot} range from this study across reported F0-F11 fumarole temperatures (Vulcano) and for Fagradallsfjall estimates of the Hg^{II}/Hg_{tot} range from (Edwards et al., 2023) (no significant difference between Hg^0 and Hg_{tot} found in near-source observations) and (Edwards et al., 2024) (1 measurement suggesting 25% of particulate bound Hg^{II} 2 km downwind).

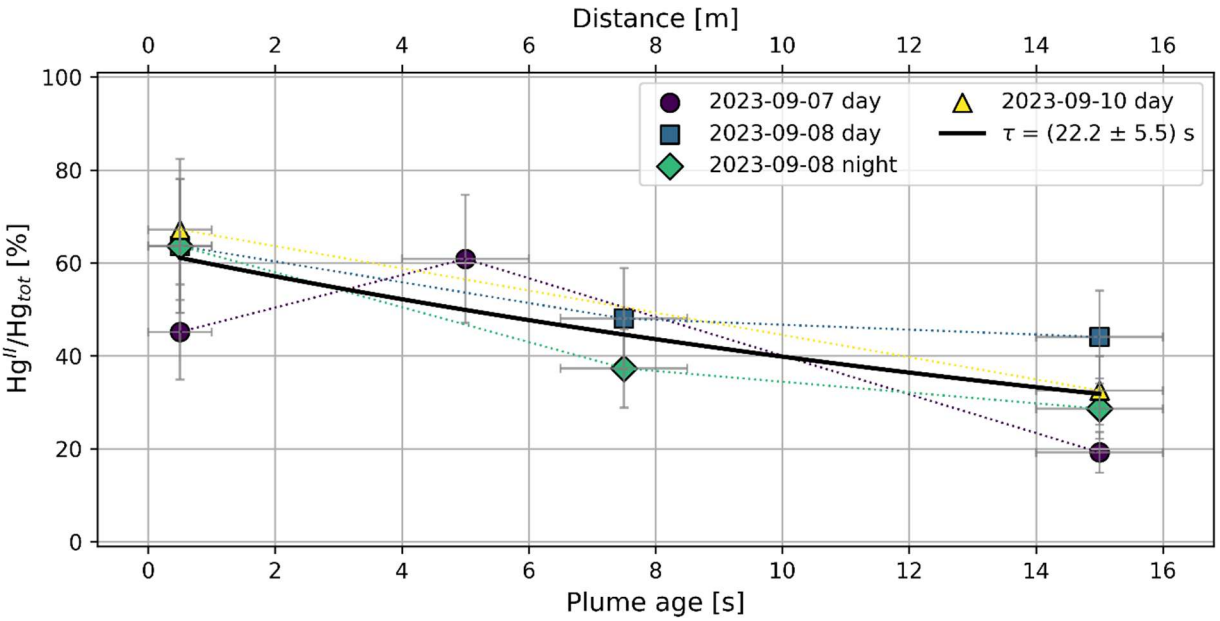

Figure 5: Hg^{II} is rapidly depleted during early plume evolution

Hg^{II}/Hg_{tot} ratio in % plotted as a function of plume age (distance on second x-axis). Different markers correspond to different measurement days. Measurements are performed simultaneously in different distances from the emission source and plume age is calculated according to a windspeed of 1 m/s. Error-bars are given based on uncertainty estimations of the distance determination. The black line corresponds to an exponential decay fit with a lifetime of Hg^{II} of (22.2 ± 5.5) s. The lifetime ranges from 7 s to approximately 44 s for windspeeds between 0.5 to 3 m/s (see Supplementary Figure S 12 and Figure S 13).

Funding
This work was supported by Le STUDIUM Loire Valley Institute for Advanced Studies through the International Consortium Project H'allo Volcano! and by the French National Research Agency (ANR) under grants ANR-18-CE01-0018 (VOLC-HAL-CLIM), ANR-10-LABX-0100 (Labex VOLTAIRE), and ANR-25-CE01-2442 (HALLOVOLCANO).

Declaration of generative AI and AI-assisted technologies in the manuscript preparation process
During the preparation of this manuscript, ChatGPT (OpenAI) was used solely for language editing and improving clarity and readability; all scientific content, analysis, interpretation, and conclusions were generated and verified by the authors.

Author contributions
Conceptualization: AN, JS, and TJR. Methodology: AN, JK, JS, and TJR. Software: AN, JK, GD, and TJR. Formal analysis: AN, BG, JS, and TJR. Investigation: AN, JK, BG, JS, NB, LS, and TJR. Writing—original draft: AN, JK, and TJR. Writing—review and editing: AN, JK, BG, JS, NB, GD, TH, LS, and TJR. Visualization: A.N. Supervision: JK and TJR.

References

Aiuppa, A., Bagnato, E., Witt, M.L.I., Mather, T.A., Parello, F., Pyle, D.M., Martin, R.S., 2007. Real-time simultaneous detection of volcanic Hg and SO2 at La Fossa Crater, Vulcano (Aeolian Islands, Sicily). Geophys. Res. Lett. 34. https://doi.org/10.1029/2007GL030762

Bagnato, E., Aiuppa, A., Parello, F., Calabrese, S., D'Alessandro, W., Mather, T.A., McGonigle, A.J.S., Pyle, D.M., Wängberg, I., 2007. Degassing of gaseous (elemental and reactive) and particulate mercury from Mount Etna volcano (Southern Italy). Atmos. Environ. 41, 7377–7388. https://doi.org/10.1016/j.atmosenv.2007.05.060

Bedjanian, Y., 2022. Experimental Study of the Reaction of O(^{3} P) with Carbonyl Sulfide between 220 and 960 K. J. Phys. Chem. A 126, 4080–4086. https://doi.org/10.1021/acs.jpca.2c02787

Bedjanian, Y., 2021. Rate Constant of the Reaction of OH Radicals with HBr over the Temperature Range 235–960 K. J. Phys. Chem. A 125, 1754–1759. https://doi.org/10.1021/acs.jpca.1c00251

Bichler, M., Poljanc, K., Sortino, F., 1995. Determination and speciation of minor and trace elements in volcanic exhalations by NAA. J. Radioanal. Nucl. Chem. Artic. 192, 183–194. https://doi.org/10.1007/BF02041722

Bobrowski, N., Hönninger, G., Galle, B., Platt, U., 2003. Detection of bromine monoxide in a volcanic plume. Nature 423, 273–276. https://doi.org/10.1038/nature01625

Bobrowski, N., von Glasow, R., Aiuppa, A., Inguaggiato, S., Louban, I., Ibrahim, O.W., Platt, U., 2007. Reactive halogen chemistry in volcanic plumes. J. Geophys. Res. Atmos. 112. https://doi.org/10.1029/2006JD007206

Cao, Y., Gao, Z., Zhu, J., Wang, Q., Huang, Y., Chiu, C., Parker, B., Chu, P., Pan, W., 2008. Impacts of Halogen Additions on Mercury Oxidation, in A Slipstream Selective Catalyst Reduction (SCR), Reactor When Burning Sub-Bituminous Coal. Environ. Sci. Technol. 42, 256–261. https://doi.org/10.1021/es071281e

Chang, L., Zhao, Y., Li, H., Tian, C., Zhang, Y., Yu, X., Zhang, J., 2017. Effect of sulfite on divalent mercury reduction and re-emission in a simulated desulfurization aqueous solution. Fuel Process. Technol. 165, 138–144. https://doi.org/10.1016/j.fuproc.2017.05.016

Colom-Díaz, J.M., Millera, Á., Bilbao, R., Alzueta, M.U., 2021. New results of H2S oxidation at high pressures. Experiments and kinetic modeling. Fuel 285, 119261. https://doi.org/10.1016/j.fuel.2020.119261

Dedeurwaerder, H., Decadt, G., Baeyens, W., 1982. Estimations of mercury fluxes emitted by Mount Etna Volcano. Bull. Volcanol. 45, 191–196. https://doi.org/10.1007/BF02597729

Di Liberto, V., Nuccio, P.M., Paonita, A., 2002. Genesis of chlorine and sulphur in fumarolic emissions at Vulcano Island (Italy): assessment of pH and redox conditions in the hydrothermal system. J. Volcanol. Geotherm. Res. 116, 137–150. https://doi.org/10.1016/S0377-0273(02)00215-9

Donovan, A., Tsanev, V., Oppenheimer, C., Edmonds, M., 2014. Reactive halogens (BrO and OClO) detected in the plume of Soufrière Hills Volcano during an eruption hiatus. Geochem. Geophys. Geosystems 15, 3346–3363. https://doi.org/10.1002/2014GC005419

Edner, H., Ragnarson, P., Svanberg, S., Wallinder, E., Ferrara, R., Cioni, R., Raco, B., Taddeucci, G., 1994. Total fluxes of sulfur dioxide from the Italian volcanoes Etna, Stromboli, and Vulcano measured by differential absorption lidar and passive differential optical absorption spectroscopy. J. Geophys. Res. Atmos. 99, 18827–18838. https://doi.org/10.1029/94JD01515

Edwards, B.A., Kushner, D.S., Outridge, P.M., Wang, F., 2021. Fifty years of volcanic mercury emission research: Knowledge gaps and future directions. Sci. Total Environ. 757, 143800. https://doi.org/10.1016/j.scitotenv.2020.143800

Edwards, B.A., Pfeffer, M.A., Ilyinskaya, E., Kleine-Marshall, B.I., Mandon, C.L., Cotterill, A., Aiuppa, A., Outridge, P.M., Wang, F., 2024. Exceptionally low mercury concentrations and fluxes from the 2021 and 2022 eruptions of Fagradalsfjall volcano, Iceland. Sci. Total Environ. 917, 170457. https://doi.org/10.1016/j.scitotenv.2024.170457

Edwards, B.A., Pfeffer, M.A., Jóhannsson, Þorsteinn, Outridge, P.M., Wang, F., 2023. An inter-method comparison of mercury measurements in Icelandic volcanic gases. Appl. Geochem. 152, 105654. https://doi.org/10.1016/j.apgeochem.2023.105654

Ferrara, R., Mazzolai, B., Lanzillotta, E., Nucaro, E., Pirrone, N., 2000. Volcanoes as emission sources of atmospheric mercury in the Mediterranean basin. Sci. Total Environ. 259, 115–121. https://doi.org/10.1016/S0048-9697(00)00558-1

Gerlach, T.M., 2004. Volcanic sources of tropospheric ozone-depleting trace gases. Geochem. Geophys. Geosystems 5. https://doi.org/10.1029/2004GC000747

Geyman, B.M., Thackray, C.P., Jacob, D.J., Sunderland, E.M., 2023. Impacts of Volcanic Emissions on the Global Biogeochemical Mercury Cycle: Insights From Satellite Observations and Chemical Transport Modeling. Geophys. Res. Lett. 50, e2023GL104667. https://doi.org/10.1029/2023GL104667

Giggenbach, W.F., Tedesco, D., Sulistiyo, Y., Caprai, A., Cioni, R., Favara, R., Fischer, T.P., Hirabayashi, J.-I., Korzhinsky, M., Martini, M., Menyailov, I., Shinohara, H., 2001. Evaluation of results from the fourth and fifth IAVCEI field workshops on volcanic gases, Vulcano island, Italy and Java, Indonesia. J. Volcanol. Geotherm. Res. 108, 157–172. https://doi.org/10.1016/S0377-0273(00)00283-3

Heimbürger, L.-E., Sonke, J.E., Cossa, D., Point, D., Lagane, C., Laffont, L., Galfond, B.T., Nicolaus, M., Rabe, B., van der Loeff, M.R., 2015. Shallow methylmercury production in the marginal sea ice zone of the central Arctic Ocean. Sci. Rep. 5, 10318. https://doi.org/10.1038/srep10318

Horowitz, H.M., Jacob, D.J., Zhang, Y., Dibble, T.S., Slemr, F., Amos, H.M., Schmidt, J.A., Corbitt, E.S., Marais, E.A., Sunderland, E.M., 2017. A new mechanism for atmospheric mercury redox chemistry: implications for the global mercury budget. Atmos. Chem. Phys. 17, 6353–6371. https://doi.org/10.5194/acp-17-6353-2017

Hsu, C.-J., Atkinson, J.D., Chung, A., Hsi, H.-C., 2021. Gaseous mercury re-emission from wet flue gas desulfurization wastewater aeration basins: A review. J. Hazard. Mater. 420, 126546. https://doi.org/10.1016/j.jhazmat.2021.126546

Hughes, K.J., Ma, L., Porter, R.T.J., Pourkashanian, M., 2011. Mercury Transformation Modelling with Bromine Addition in Coal Derived Flue Gases, in: Pistikopoulos, E.N., Georgiadis, M.C., Kokossis, A.C. (Eds.), Computer Aided Chemical Engineering. Presented at the 21 European Symposium on Computer Aided Process Engineering, Elsevier, pp. 171–175. https://doi.org/10.1016/B978-0-444-53711-9.50035-3

Karbach, N., Bobrowski, N., Hoffmann, T., 2022. Observing volcanoes with drones: studies of volcanic plume chemistry with ultralight sensor systems. Sci. Rep. 12, 17890. https://doi.org/10.1038/s41598-022-21935-5

Kelly, P.J., Kern, C., Roberts, T.J., Lopez, T., Werner, C., Aiuppa, A., 2013. Rapid chemical evolution of tropospheric volcanic emissions from Redoubt Volcano, Alaska, based on observations of ozone and halogen-containing gases. J. Volcanol. Geotherm. Res. 259, 317–333. https://doi.org/10.1016/j.jvolgeores.2012.04.023

Koenig, A.M., Magand, O., Rose, C., Muro, A.D., Miyazaki, Y., Colomb, A., Rissanen, M., F. Lee, C., K. Koenig, T., Volkamer, R., Brioude, J., Verreyken, B., Roberts, T., A. Edwards, B., Sellegri, K., Arellano, S., Kowalski, P., Aiuppa, A., E. Sonke, J., Dommergue, A., 2023. Observed in-plume gaseous elemental mercury depletion suggests significant mercury scavenging by volcanic aerosols. Environ. Sci. Atmos. 3, 1418–1438. https://doi.org/10.1039/D3EA00063J

Krzyżyńska, R., Szeliga, Z., Pilar, L., Borovec, K., Regucki, P., 2020. High mercury emission (both forms: Hg0 and Hg2+) from the wet scrubber in a full-scale lignite-fired power plant. Fuel 270, 117491. https://doi.org/10.1016/j.fuel.2020.117491

Kuhn, J., Bobrowski, N., Platt, U., 2022. The Interface Between Magma and Earth's Atmosphere. Geochem. Geophys. Geosystems 23. https://doi.org/10.1029/2022GC010671

Kushner, D.S., Lopez, T.M., Wallace, K.L., Damby, D.E., Kern, C., Cameron, C.E., 2023. Estimates of volcanic mercury emissions from Redoubt Volcano, Augustine Volcano, and Mount Spurr eruption ash. Front. Earth Sci. 11, 1054521. https://doi.org/10.3389/feart.2023.1054521

Li, C., Sonke, J.E., Le Roux, G., Piotrowska, N., Van Der Putten, N., Roberts, S.J., Daley, T., Rice, E., Gehrels, R., Enrico, M., Mauquoy, D., Roland, T.P., De Vleeschouwer, F., 2020. Unequal Anthropogenic Enrichment of Mercury in Earth's Northern and Southern Hemispheres. ACS Earth Space Chem. 4, 2073–2081. https://doi.org/10.1021/acsearthspacechem.0c00220

Martin, R.S., Mather, T.A., Pyle, D.M., 2006. High-temperature mixtures of magmatic and atmospheric gases. Geochem. Geophys. Geosystems 7. https://doi.org/10.1029/2005GC001186

Martin, R.S., Witt, M.L.I., Pyle, D.M., Mather, T.A., Watt, S.F.L., Bagnato, E., Calabrese, S., 2011. Rapid oxidation of mercury (Hg) at volcanic vents: Insights from high temperature thermodynamic models of Mt Etna's emissions. Chem. Geol. 283, 279–286. https://doi.org/10.1016/j.chemgeo.2011.01.027

Miller, T.P., McGimsey, R.G., Richter, D.H., Riehle, J.R., Nye, C.J., Yount, M.E., Dumoulin, J.A., 1998. Catalog of the historically active volcanoes of Alaska (Open-File Report), Open-File Report. USGS.

Neri, A., Barberi, F., Carapezza, M.L., 2025. Lessons from the 2021–2023 unrest crisis on Vulcano (Italy). Bull. Volcanol. 87, 79. https://doi.org/10.1007/s00445-025-01864-7

Nies, A., Roberts, T.J., Dayma, G., Fischer, T.P., Kuhn, J., 2025. Reactive bromine in volcanic plumes confines the emission temperature and oxidation of magmatic gases at the atmospheric interface. Sci. Adv. 11, eadt8607. https://doi.org/10.1126/sciadv.adt8607

Niksa, S., Padak, B., Krishnakumar, B., Naik, C.V., 2010. Process Chemistry of Br Addition to Utility Flue Gas for Hg Emissions Control. Energy Fuels 24, 1020–1029. https://doi.org/10.1021/ef901106t

Paonita, A., Bellomo, S., Bonfanti, P., Capasso, G., Di Martino, R.M.R., Federico, C., Gattuso, A., Inguaggiato, S., Italiano, F., La Pica, L., Madonia, P., Oliveri, Y., Pecoraino, G., Pisciotta, A., Sortino, F., Tantillo, M., 2025. Chemical and isotopic data on volcanic gases from crater fumaroles on Vulcano Island (Sicily). https://doi.org/10.60520/IEDA/113739

Pavlish, J.H., Sondreal, E.A., Mann, M.D., Olson, E.S., Galbreath, K.C., Laudal, D.L., Benson, S.A., 2003. Status review of mercury control options for coal-fired power plants. Fuel Process. Technol. 82, 89–165. https://doi.org/10.1016/S0378-3820(03)00059-6

Preciado, I., Young, T., Silcox, G., 2014. Mercury Oxidation by Halogens under Air- and Oxygen-Fired Conditions. Energy Fuels 28, 1255–1261. https://doi.org/10.1021/ef402074p

Pyle, D.M., Mather, T.A., 2003. The importance of volcanic emissions for the global atmospheric mercury cycle. Atmos. Environ. 37, 5115–5124. https://doi.org/10.1016/j.atmosenv.2003.07.011

Raj, A., Ibrahim, S., Jagannath, A., 2020. Combustion kinetics of H2S and other sulfurous species with relevance to industrial processes. Prog. Energy Combust. Sci. 80, 100848. https://doi.org/10.1016/j.pecs.2020.100848

Roberts, T.J., Braban, C.F., Martin, R.S., Oppenheimer, C., Adams, J.W., Cox, R.A., Jones, R.L., Griffiths, P.T., 2009. Modelling reactive halogen formation and ozone depletion in volcanic plumes. Chem. Geol. 263, 151–163. https://doi.org/10.1016/j.chemgeo.2008.11.012

Roberts, T.J., Dayma, G., Oppenheimer, C., 2019. Reaction Rates Control High-Temperature Chemistry of Volcanic Gases in Air. Front. Earth Sci. 7, 154. https://doi.org/10.3389/feart.2019.00154

Roberts, T.J., Martin, R.S., Jourdain, L., 2014. Reactive bromine chemistry in Mount Etna's volcanic plume: the influence of total Br, high-temperature processing, aerosol loading and plume–air mixing. Atmos. Chem. Phys. 14, 11201–11219. https://doi.org/10.5194/acp-14-11201-2014

Rüdiger, J., Gutmann, A., Bobrowski, N., Liotta, M., de Moor, J.M., Sander, R., Dinger, F., Tirpitz, J.-L., Ibarra, M., Saballos, A., Martínez, M., Mendoza, E., Ferrufino, A., Stix, J., Valdés, J., Castro, J.M., Hoffmann, T., 2021. Halogen activation in the plume of Masaya volcano: field observations and box model investigations. Atmos. Chem. Phys. 21, 3371–3393. https://doi.org/10.5194/acp-21-3371-2021

Saiz-Lopez, A., Acuña, A.U., Mahajan, A.S., Dávalos, J.Z., Feng, W., Roca-Sanjuán, D., Carmona-García, J., Cuevas, C.A., Kinnison, D.E., Gómez Martín, J.C., Francisco, J.S., Plane, J.M.C., 2022. The Chemistry of Mercury in the Stratosphere. Geophys. Res. Lett. 49, e2022GL097953. https://doi.org/10.1029/2022GL097953

Saiz-Lopez, A., Acuña, A.U., Trabelsi, T., Carmona-García, J., Dávalos, J.Z., Rivero, D., Cuevas, C.A., Kinnison, D.E., Sitkiewicz, S.P., Roca-Sanjuán, D., Francisco, J.S., 2019. Gas-Phase Photolysis of Hg(I) Radical Species: A New Atmospheric Mercury Reduction Process. J. Am. Chem. Soc. 141, 8698–8702. https://doi.org/10.1021/jacs.9b02890

Schroeder, W.H., Anlauf, K.G., Barrie, L.A., Lu, J.Y., Steffen, A., Schneeberger, D.R., Berg, T., 1998. Arctic springtime depletion of mercury. Nature 394, 331–332. https://doi.org/10.1038/28530

Schroeder, W.H., Keeler, G., Kock, H., Roussel, P., Schneeberger, D., Schaedlich, F., 1995. International field intercomparison of atmospheric mercury measurement methods. Water. Air. Soil Pollut. 80, 611–620. https://doi.org/10.1007/BF01189713

Scott, S., Pfeffer, M., Oppenheimer, C., Bali, E., Lamb, O.D., Barnie, T., Woods, A.W., Kjartansdóttir, R., Stefánsson, A., 2023. Near-surface magma flow instability drives cyclic lava fountaining at Fagradalsfjall, Iceland. Nat. Commun. 14, 6810. https://doi.org/10.1038/s41467-023-42569-9

Solis, K.L.B., Nam, G., Hong, Y., 2017. Mercury(II) reduction and sulfite oxidation in aqueous systems: kinetics study and speciation modeling. Environ. Chem. 14, 151. https://doi.org/10.1071/EN16169

Steffen, A., Douglas, T., Amyot, M., Ariya, P., Aspmo, K., Berg, T., Bottenheim, J., Brooks, S., Cobbett, F., Dastoor, A., Dommergue, A., Ebinghaus, R., Ferrari, C., Gardfeldt, K., Goodsite, M.E., Lean, D., Poulain, A.J., Scherz, C., Skov, H., Sommar, J., Temme, C., 2008. A synthesis of atmospheric mercury depletion event chemistry in the atmosphere and snow. Atmos. Chem. Phys. 8, 1445–1482. https://doi.org/10.5194/acp-8-1445-2008

Sun, R., Enrico, M., Heimbürger, L.-E., Scott, C., Sonke, J.E., 2013. A double-stage tube furnace—acid-trapping protocol for the pre-concentration of mercury from solid samples for isotopic analysis. Anal. Bioanal. Chem. 405, 6771–6781. https://doi.org/10.1007/s00216-013-7152-2

Surl, L., Roberts, T., Bekki, S., 2021. Observation and modelling of ozone-destructive halogen chemistry in a passively degassing volcanic plume. Atmos. Chem. Phys. 21, 12413–12441. https://doi.org/10.5194/acp-21-12413-2021

Von Glasow, R., 2010. Atmospheric chemistry in volcanic plumes. Proc. Natl. Acad. Sci. 107, 6594–6599. https://doi.org/10.1073/pnas.0913164107

Wallace, K., Neal, C., McGimsey, R., 2010. Timing, distribution, and character of tephra fall from the 2005-2006 eruption of Augustine Volcano (Professional Paper), Professional Paper.

Wallace, K.L., Schaefer, J.R., Coombs, M.L., 2013. Character, mass, distribution, and origin of tephra-fall deposits from the 2009 eruption of Redoubt Volcano, Alaska—Highlighting the significance of particle aggregation. J. Volcanol. Geotherm. Res. 259, 145–169. https://doi.org/10.1016/j.jvolgeores.2012.09.015

Wang, S., McNamara, S.M., Moore, C.W., Obrist, D., Steffen, A., Shepson, P.B., Staebler, R.M., Raso, A.R.W., Pratt, K.A., 2019. Direct detection of atmospheric atomic bromine leading to mercury and ozone depletion. Proc. Natl. Acad. Sci. 116, 14479–14484. https://doi.org/10.1073/pnas.1900613116

Werner, C., Kelly, P.J., Doukas, M., Lopez, T., Pfeffer, M., McGimsey, R., Neal, C., 2013. Degassing of CO2, SO2, and H2S associated with the 2009 eruption of Redoubt Volcano, Alaska. J. Volcanol. Geotherm. Res. 259, 270–284. https://doi.org/10.1016/j.jvolgeores.2012.04.012

Witt, M.L.I., Mather, T.A., Pyle, D.M., Aiuppa, A., Bagnato, E., Tsanev, V.I., 2008. Mercury and halogen emissions from Masaya and Telica volcanoes, Nicaragua. J. Geophys. Res. Solid Earth 113. https://doi.org/10.1029/2007JB005401

Wittmer, J., Bobrowski, N., Liotta, M., Giuffrida, G., Calabrese, S., Platt, U., 2014. Active alkaline traps to determine acidic-gas ratios in volcanic plumes: Sampling techniques and analytical methods. Geochem. Geophys. Geosystems 15, 2797–2820. https://doi.org/10.1002/2013GC005133

Yang, Y., Liu, J., Wang, Z., 2020. Reaction mechanisms and chemical kinetics of mercury transformation during coal combustion. Prog. Energy Combust. Sci. 79, 100844. https://doi.org/10.1016/j.pecs.2020.100844

Yang, Y., Liu, J., Wang, Z., Zhang, Z., 2017. Homogeneous and heterogeneous reaction mechanisms and kinetics of mercury oxidation in coal-fired flue gas with bromine addition. Proc. Combust. Inst. 36, 4039–4049. https://doi.org/10.1016/j.proci.2016.08.068

Zambardi, T., Sonke, J.E., Toutain, J.P., Sortino, F., Shinohara, H., 2009. Mercury emissions and stable isotopic compositions at Vulcano Island (Italy). Earth Planet. Sci. Lett. 277, 236–243. https://doi.org/10.1016/j.epsl.2008.10.023

Zeng, Z., Dlugogorski, B.Z., Oluwoye, I., Altarawneh, M., 2021. Combustion chemistry of COS and occurrence of intersystem crossing. Fuel 283, 119257. https://doi.org/10.1016/j.fuel.2020.119257

Zhou, Y., Li, Y., Zheng, W., Tang, S., Pan, S., Chen, J., He, X.-F., Shen, J., Algeo, T.J., 2024. The role of LIPs in Phanerozoic mass extinctions: An Hg perspective. Earth-Sci. Rev. 249, 104667. https://doi.org/10.1016/j.earscirev.2023.104667

Supplementary Material

Table S 1: Overview over the field campaign data from the 2019 and 2023 campaigns at La Fossa carter on Vulcano island. Breakthrough tests were performed on 2023-09-10/12, yielding around 3% breakthrough for the AC traps and around 7% for the PES filters.

Date [yyyy-mm-dd]	Fumarole	Daytime	Sampling time [min]	d [m]	Hg^0 [ng/m³]	ΔHg^0[ng/m³]	Hg^{II} [ng/m³]	ΔHg^{II} [ng/m³]	Hg_{tot} [ng/m³]	ΔHg_{tot} [ng/m³]	SO_2 [ng/m³]	ΔSO_2 [ng/m³]	SO_2^{std} [ng/m³]
2019-09-24	F0	day	239	5	4.4	0.704	8.7	1.392	13.1	2.096	/	/	/
2019-09-24	F0	day	68	5	/	/	4.1	0.656	/	/	/	/	/
2019-09-25	F0	day	200	5	2.3	0.368	13	2.08	15.3	2.448	/	/	/
2019-09-25	F0	day	183	5	9.7	1.552	34.2	5.472	43.9	7.024	/	/	/
2019-09-25	F0	day	187	5	4.1	0.656	4.7	0.752	8.8	1.408	/	/	/
2019-09-25	F0	night	214	5	10.4	1.664	1.9	0.304	12.3	1.968	/	/	/
2019-09-25	F0	night	183	5	2.8	0.448	5.7	0.912	8.5	1.36	/	/	/
2023-09-07	F0	day	45	0	158	25.28	130	20.8	288	46.08	4.69E+08	5206261	2.55E+08
2023-09-07	F0	day	35	0	/	/	152	24.32	/	/	6.43E+08	5206261	2.94E+08
2023-09-07	F0	day	70	0	/	/	131	20.96	/	/	5.7E+08	5206261	2.66E+08
2023-09-07	F0	day	135	5	9	1.44	14	2.24	23	3.68	61173570	520626.1	44253221
2023-09-07	F0	day	135	10	7.7	1.232	/	/	/	/	19106979	156187.8	15098158
2023-09-07	F0	day	125	15	8.4	1.344	2	0.32	10.4	1.664	21710109	156187.8	13015653
2023-09-08	F0	day	238	0	129.6	20.736	227	36.32	356.6	57.056	4.27E+08	2603131	1.67E+08
2023-09-08	F0	day	240	7.5	49.8	7.968	46	7.36	95.8	15.328	1.63E+08	1041252	1.17E+08
2023-09-08	F0	day	242	15	38.1	6.096	30	4.8	68.1	10.896	1.05E+08	1041252	1.35E+08
2023-09-08	F0	night	183	0	153.3	24.528	268	42.88	421.3	67.408	4.14E+08	2603131	1.43E+08
2023-09-08	F0	night	177	7.5	31.9	5.104	19	3.04	50.9	8.144	2.79E+08	780939.2	72887658
2023-09-08	F0	night	183	15	74.8	11.968	30	4.8	104.8	16.768	1.66E+08	260313.1	33840698
2023-09-09	F0	day	190	/	6	0.96	2	0.32	8	1.28	22126610	260313.1	20825045
2023-09-09	F8/9	day	163	/	9.6	1.536	2	0.32	11.6	1.856	72887658	780939.2	65078266
2023-09-09	F11	day	230	/	11	1.76	/	/	/	/	1.31E+08	520626.1	57268874
2023-09-09	F0	night	200	/	41.7	6.672	8	1.28	49.7	7.952	72106718	520626.1	59872005
2023-09-09	F8/9	night	200	/	45.7	7.312	102	16.32	147.7	23.632	73147971	520626.1	59872005
2023-09-09	F0	night	195	/	83	13.28	70	11.2	153	24.48	1.62E+08	780939.2	91109572
2023-09-10	F0	day	125	0	83	13.28	170	27.2	253	40.48	7.24E+08	2603131	2.94E+08
2023-09-10	F0	day	145	0	96.7	15.472	/	/	/	/	3.88E+08	2603131	2.26E+08
2023-09-10	F0	day	125	15	45.6	7.296	22	3.52	67.6	10.816	1.37E+08	1041252	78093919

2023-09-12	F0	day	185	/	20.4	3.264	10	1.6	30.4	4.864	84341432	520626.1	41650090
2023-09-12	F0	day	185	/	29.7	4.752	1	0.16	30.7	4.912	79916110	520626.1	49459482

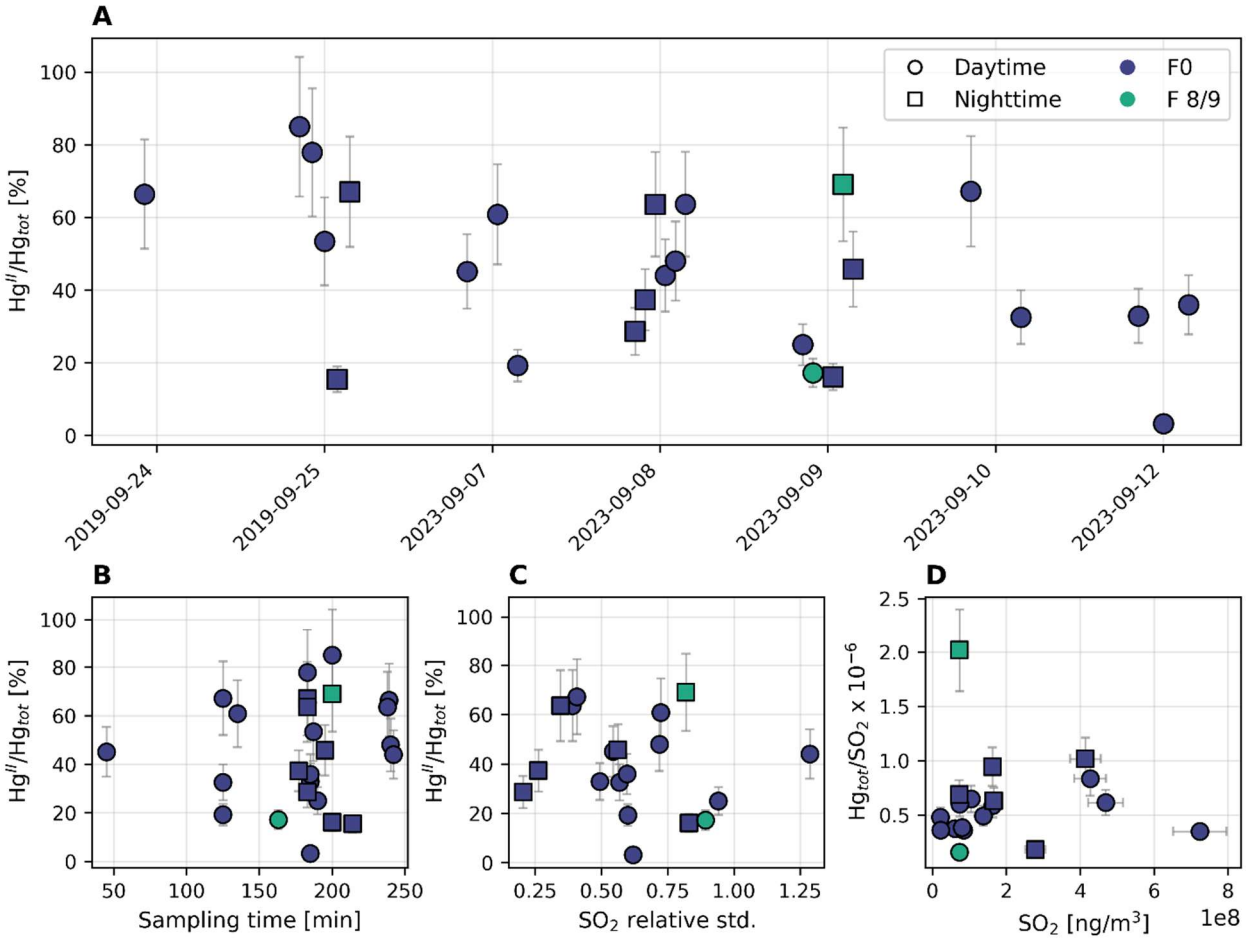

Figure S 1: Overview over all Hg^{II}/Hg_{tot} ratios in % obtained during the two field campaigns highlighted in this work in September 2019 and 2023 (A). The second row shows various tests to assess trends in the data and for quality control. Plot B shows the Hg^{II}/Hg_{tot} ratio in % against the total sampling time to assess if the there is a bias caused by sampling time. Plot C shows the Hg^{II}/Hg_{tot} ratio in % against the relative standard deviation of the SO_2 measurement, which investigates sampling biases due to varying plume exposure (high relative std. is indicative of a high plume variability during sampling) and lastly plot D shows the ratio between Hg_{tot}/SO_2 over distance parameterized by SO_2 concentration, finding no biases with plume SO_2 concentration.

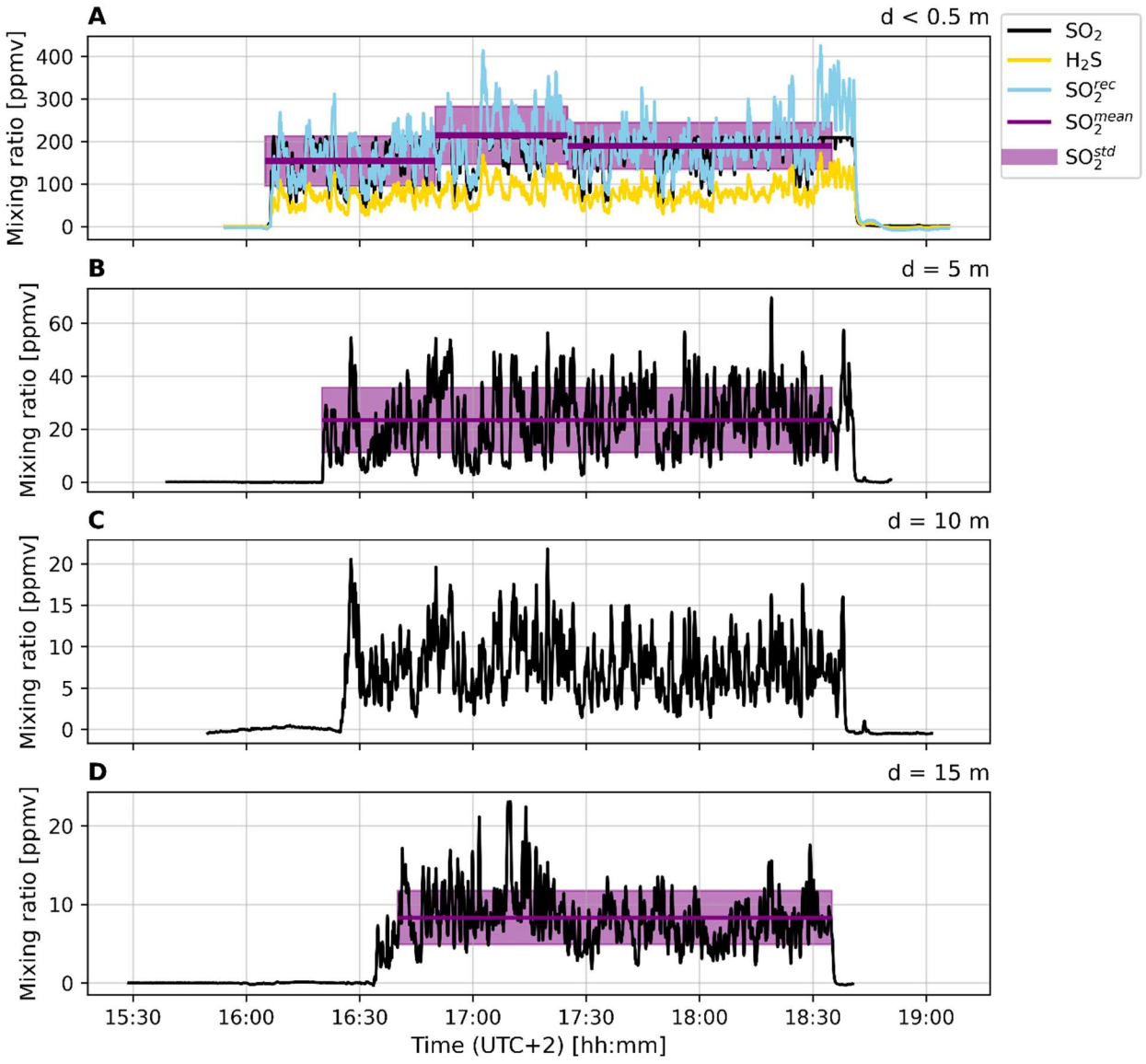

Figure S 2: SO_2 measurements performed on 2023-09-07 at fumarole F0 in different distances from the emission. Measurements are performed at four distances indicated by the title: at-source (< 0.5 m) 5 m, 10 m, and 15 m. For the closest sensor set (d < 0.5 m), the SO_2 sensor reaches saturation at 200 ppmv, and the signal is recovered ($SO_2^{rec.}$, blue line) using a co-deployed H_2S sensor with lower saturation limit (yellow line), and under a broadly constant H_2S/SO_2 ratio of the emission, yielding excellent agreement with the SO_2, sensor and peaks up to 400 ppmv. The purple horizontal lines indicate the average SO_2 mixing ratio during Hg sampling and the shaded area shows the standard deviation of the average. The measurement at d = 10 m did not result in a valid Hg measurement and therefore sampling time and SO_2 average are not indicated here, it simply shows the dilution trend over distance. For the at-source Hg measurement, three consecutive samples were taken to avoid severe PES filter clogging by high humidity close to the emission source.

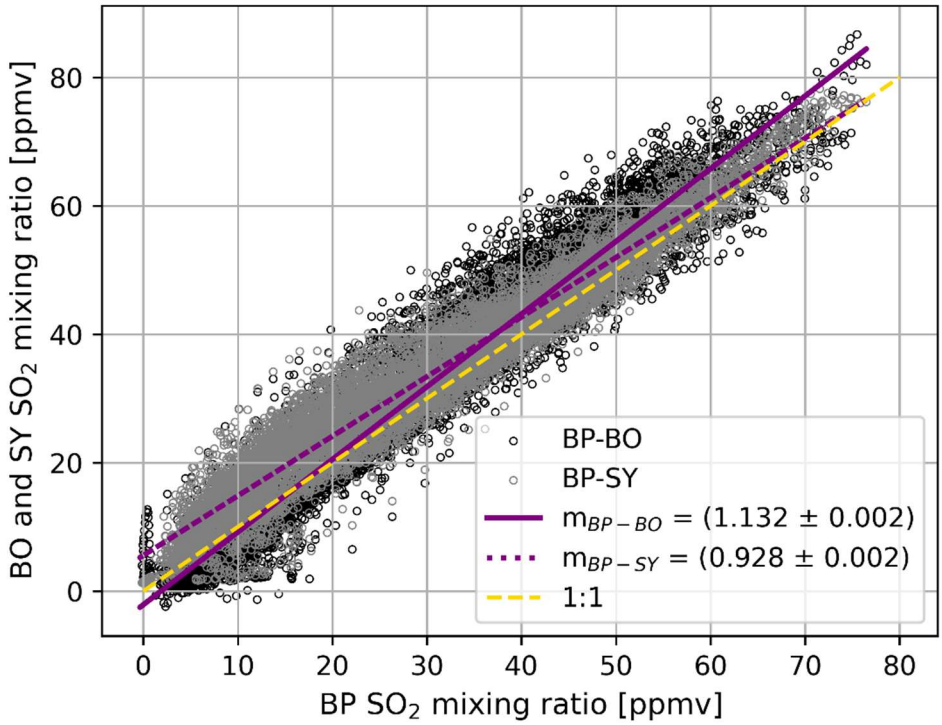

Figure S 3: Estimation of calibration error through cross-comparison of three SO_2 sensor systems (BP, BO, and SY) that were co-located for 185 min (between 10:05 and 13:10 (UTC+2)) on 2023-09-12. The dots show the response time corrected SO_2 mixing ratios in ppmv during the co-location period and the gold dotted line shows a 1:1 line for reference. The two purple lines show linear regressions of the datapoints with $R^2_{BP\text{-}BO}$ = 0.73 and $R^2_{BP\text{-}SY}$ = 0.94. According to the slopes the BO sensor system overestimates BP by around 13% whereas SY shows a slight underestimation by around 7% to the BP system. Thus, overall, an error of for the SO_2 values of $\pm$ 10% is assumed for all measurements, far exceeding the statistical error for the long averaging periods of the Hg measurements.

Gas compositions used for the model simulation study

For the model sensitivity study three different volcanic gas compositions are explored. First from fumaroles at La Fossa crater on Vulcano island (Sicily, Italy), in particular for fumarole F0 (Aiuppa et al., 2007). The other two compositions are plume gases from lager eruptions. Second the plume of Redoubt volcano (Alaska, USA) (Gerlach, 2004; Kelly et al., 2013; Werner et al., 2013), and third the plume from Fagradalsfjall (Iceland) (Scott et al., 2023). Model simulations are initialized where possible with measured compositions. In the case of Vulcano the reported gas composition was measured at-source by inserting tubes and sampling the gases before interaction with atmospheric air (Aiuppa et al., 2007). These measurements are supplemented by results from the 2023 measurement campaign for halogens (Br and Cl) measured by an alkaline trap and mercury. For the Redoubt and Fagradalsfjall cases, direct at-source measurements were not available. Therefore the gas composition is estimated from plume gas ratios measured in the downwind plume by (Werner et al., 2013) and (Kelly et al., 2013) for Redoubt and (Scott et al., 2023) for Fagradalsfjall. Water vapor mixing ratios are estimated to be around 0.90 typical for many volcanic emissions worldwide (see e.g. (Gerlach, 2004)). Additionally, in the Redoubt case, CO_2 and HBr (through the Br/Cl ratio) have been estimated from the *arcmean* composition by (Gerlach, 2004) which allows to calculate several other species according to their ratio to CO_2. If not reported or measured, reduced gases are calculated according to reported Nickel-Nickel-Oxide (NNO) redox buffer in combination with the emission temperature (NNO + 1.5 for Redoubt (Werner et al., 2013) and NNO – 0.07 for Fagradalsfjall (Scott et al., 2023)). Further, initial radical species such as OH, H, Br and Cl are calculated as thermochemical equilibrium at the magmatic gas emission temperature, which deliver a significant contribution only for the high-temperature plume compositions from Redoubt and Fagradalsfjall.

Table S 2: Summary of gas compositions used in the model study. Values marked with an asterisk are calculated, values marked with a double asterisk are estimated, and all other values are obtained from the literature as discussed above.

Volcano	**Vulcano fumarole F0**					**Redoubt plume**		**Fagradalsfjall plume**		
T [K]	560	660	760	460	360	1273	998	1473	1273	1073
H_2O [mol/mol]	0.90	0.90	0.90	0.90	0.90	0.90**	0.90**	0.90**	0.90**	0.90**
CO_2 [mol/mol]	0.095	0.095	0.095	0.095	0.095	0.046**	0.046**	0.078	0.078	0.078
SO_2 [mol/mol]	0.0034	0.0034	0.0034	0.0034	0.0034	0.014	0.014	0.023	0.023	0.023
H_2S [mol/mol]	0.0016	0.0016	0.0016	0.0016	0.0016	0.0011	0.0011	0.00015	0.00015	0.00015
HCl [mol/mol]	0.0020	0.0020	0.0020	0.0020	0.0020	0.0095	0.0095	0.00080	0.00080	0.00080
HBr [mol/mol]	9.0×10^{-7}	9.0×10^{-7}	9.0×10^{-7}	9.0×10^{-7}	9.0×10^{-7}	2.1×10^{-5}**	2.1×10^{-5}**	1.7×10^{-6}	1.7×10^{-6}	1.7×10^{-6}
H_2 [mol/mol]	3.2×10^{-5}	3.2×10^{-5}	3.2×10^{-5}	3.2×10^{-5}	3.2×10^{-5}	0.00087*	0.00070*	0.0059*	0.0053*	0.0046*

CO [mol/mol]	4.8×10^{-7}	4.8×10^{-7}	4.8×10^{-7}	4.8×10^{-7}	4.8×10^{-7}	0.00010*	3.0×10^{-5}*	6.0×10^{-5}	6.0×10^{-5}	6.0×10^{-5}
OH [mol/mol]	< 1.0×10^{-12}	< 1.0×10^{-12}	< 1.0×10^{-12}	< 1.0×10^{-12}	< 1.0×10^{-12}	1.9×10^{-7}*	1.7×10^{-10}*	5.7×10^{-6}*	1.5×10^{-7}*	1.3×10^{-9}*
H [mol/mol]	< 1.0×10^{-12}	< 1.0×10^{-12}	< 1.0×10^{-12}	< 1.0×10^{-12}	< 1.0×10^{-12}	5.0×10^{-8} *	1.0×10^{-10}*	7.9×10^{-7}*	4.4×10^{-8}*	6.4×10^{-10}*
Br [mol/mol]	< 1.0×10^{-12}	< 1.0×10^{-12}	< 1.0×10^{-12}	< 1.0×10^{-12}	< 1.0×10^{-12}	8.8×10^{-8}*	2.5×10^{-9}*	3.8×10^{-8}*	5.4×10^{-9}*	5.0×10^{-10}*
Cl [mol/mol]	< 1.0×10^{-12}	< 1.0×10^{-12}	< 1.0×10^{-12}	< 1.0×10^{-12}	< 1.0×10^{-12}	1.3×10^{-7}*	6.2×10^{-10}*	1.4×10^{-7}*	8.1×10^{-9}*	2.3×10^{-10}*
Hg [mol/mol]	7.5×10^{-10}	7.5×10^{-10}	7.5×10^{-10}	7.5×10^{-10}	7.5×10^{-10}	1.4×10^{-7}	1.4×10^{-7}	4.1×10^{-10}	4.1×10^{-10}	4.1×10^{-10}
Hg/SO_2	2.2×10^{-7}	2.2×10^{-7}	2.2×10^{-7}	2.2×10^{-7}	2.2×10^{-7}	1.0×10^{-5}**	1.0×10^{-5}**	1.8×10^{-8}	1.8×10^{-8}	1.8×10^{-8}

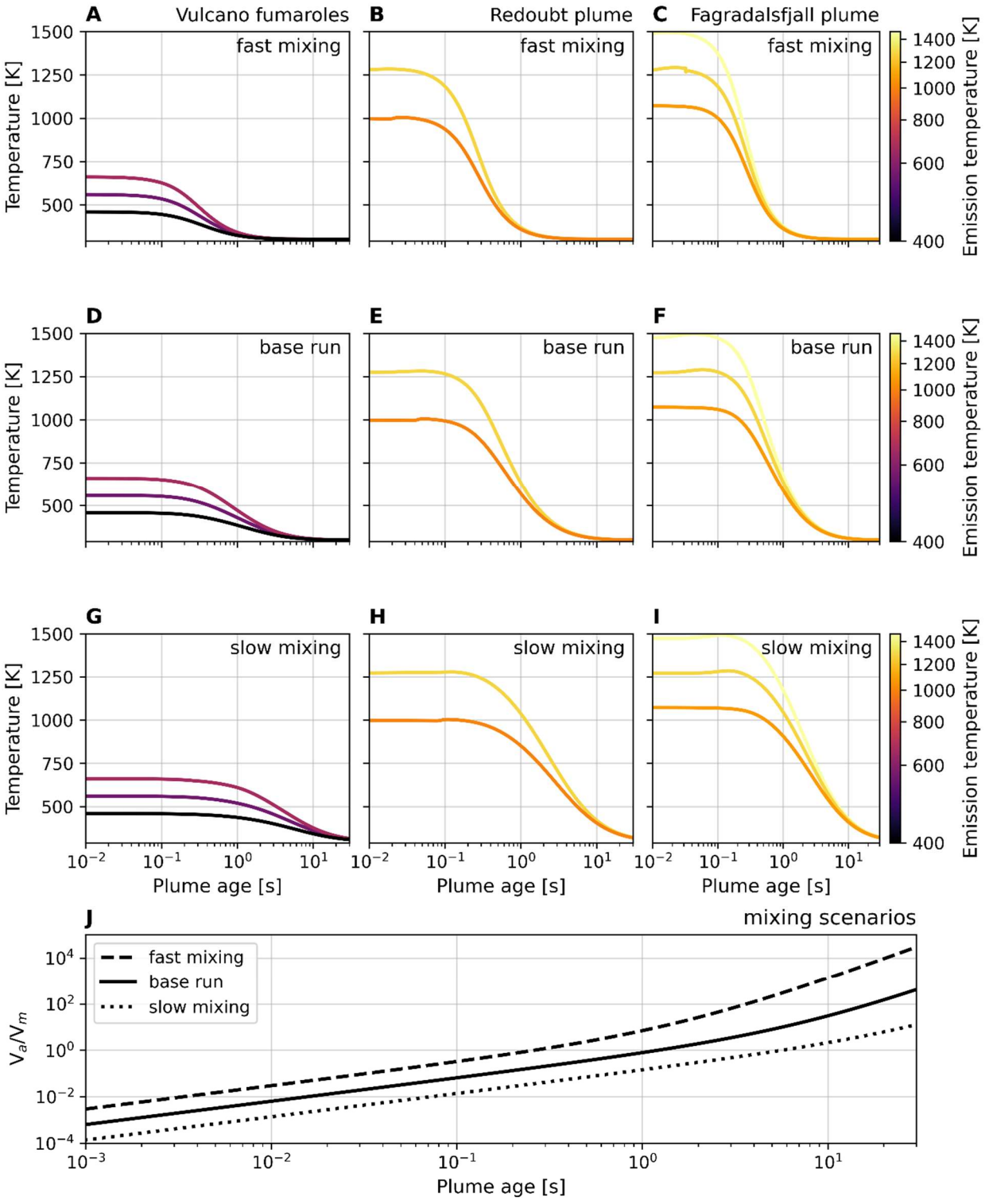

Figure S 4: Physical parameters of the model simulations presented in section 3.2. Panel A-I shows the plume temperature evolution for the three volcanic case studies (and their emission temperature estimates, see text) for every mixing scenario (base run, x100 higher and x100 lower mixing rate). Mixing scenarios are indicated in Panel J through the ratio between atmospheric air (V_a) to magmatic gas (V_m).

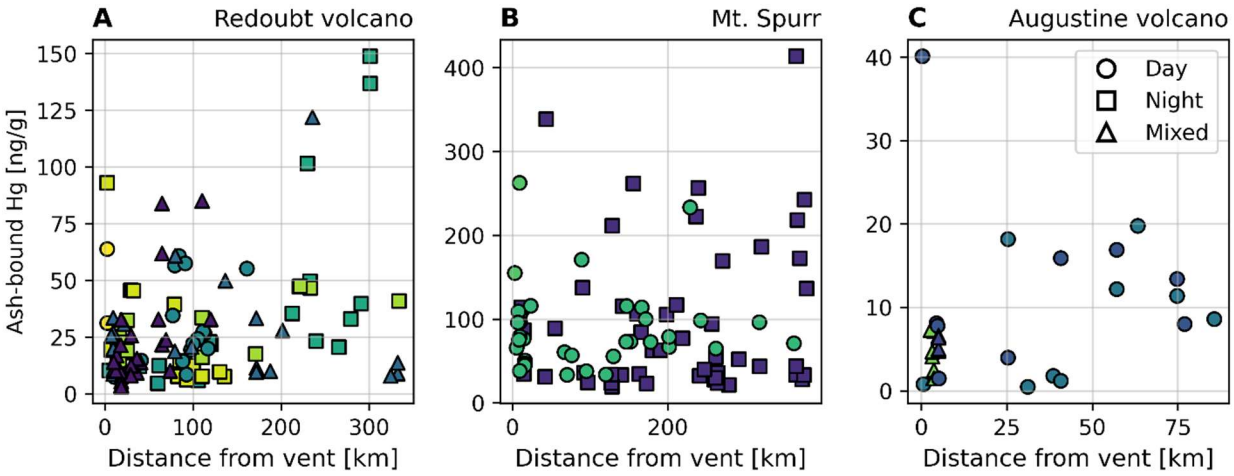

Figure S 5: Reanalysis of (Kushner et al., 2023) ash-bound Hg measurements sorted after day, night and mixed (i.e. day and night, or uncertain) eruption times as indicated by the marker, plotted as a function of distance downwind following (Kushner et al., 2023). The color filling of the marker indicates different eruptive events. As shown by (Kushner et al., 2023), the three volcanoes exhibit distinct mercury contents and include samples with high Hg very near source. No consistent trends are evidenced as a function of distance from vent for the day/night/mixed eruption time categorized data, consistent with the findings of (Kushner et al., 2023) who concluded that mercury oxidation and adsorption to ash occurs on sub-minute timescales.

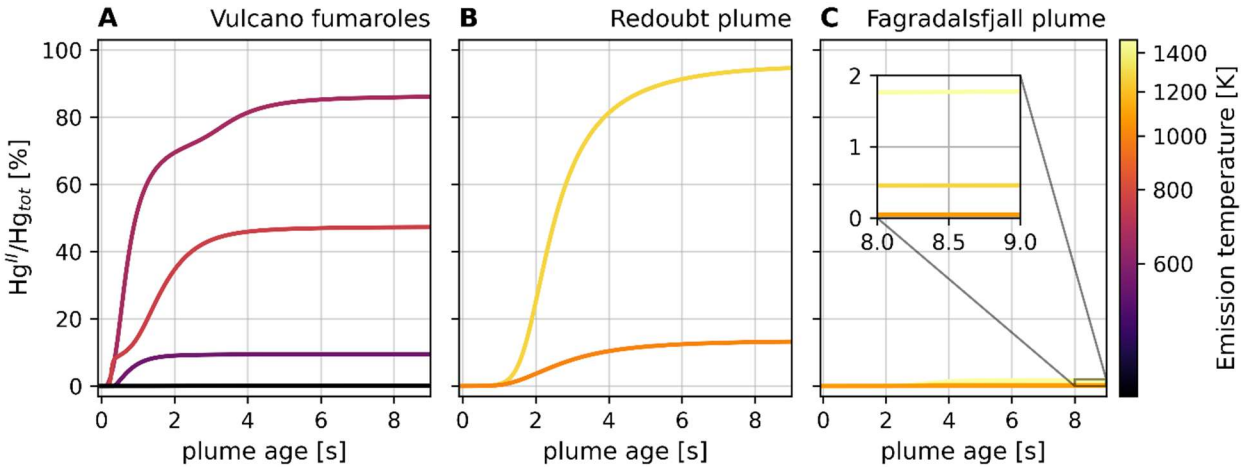

Figure S 6: Model results of the emission temperature sensitivity study for the base run mixing scenario. Percentage of total mercury in the form Hg^{II} simulated over 9 s for halogen-rich Vulcano, Mt Redoubt and halogen-poor Fagradalsfjall plumes.

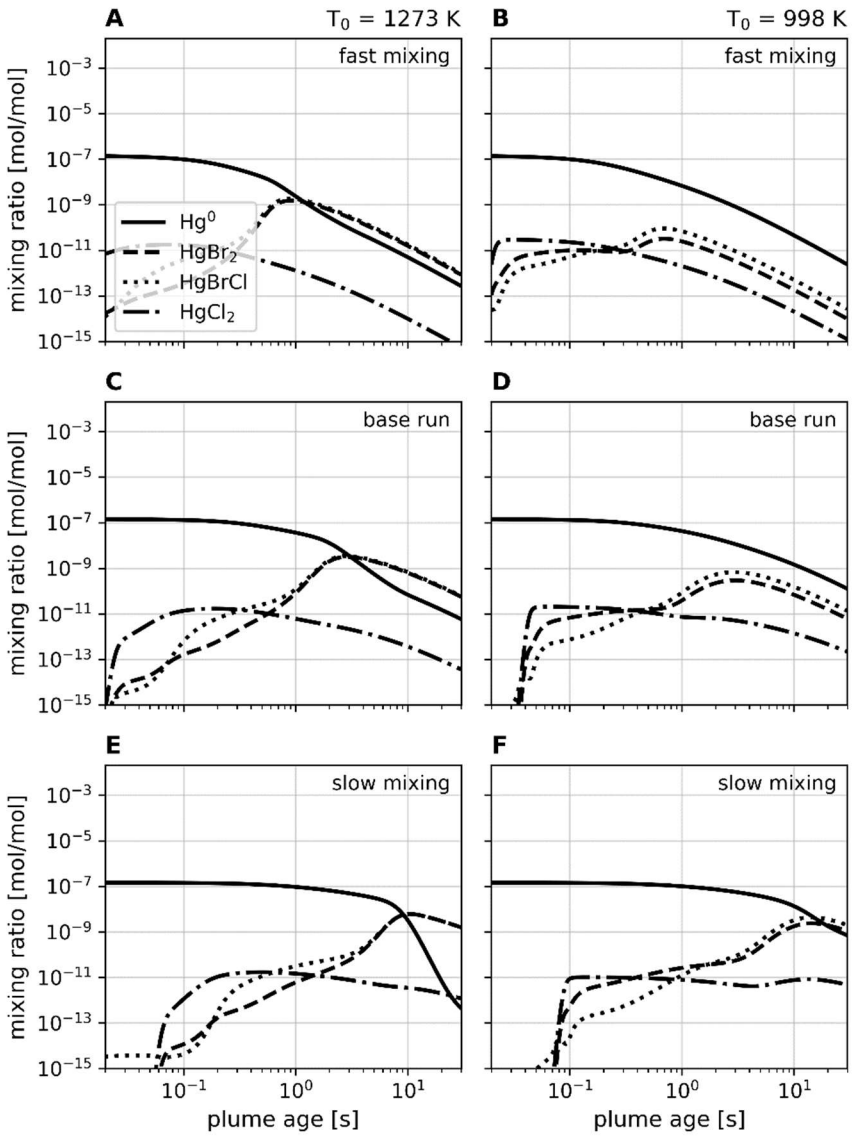

Figure S 7: Hg speciation for the Redoubt plume case study for two emissions temperatures (T_0 = 1273 K, 998 K) and three mixing scenarios. Shown are the dominant Hg^{II} species and the primary emitted Hg^0.

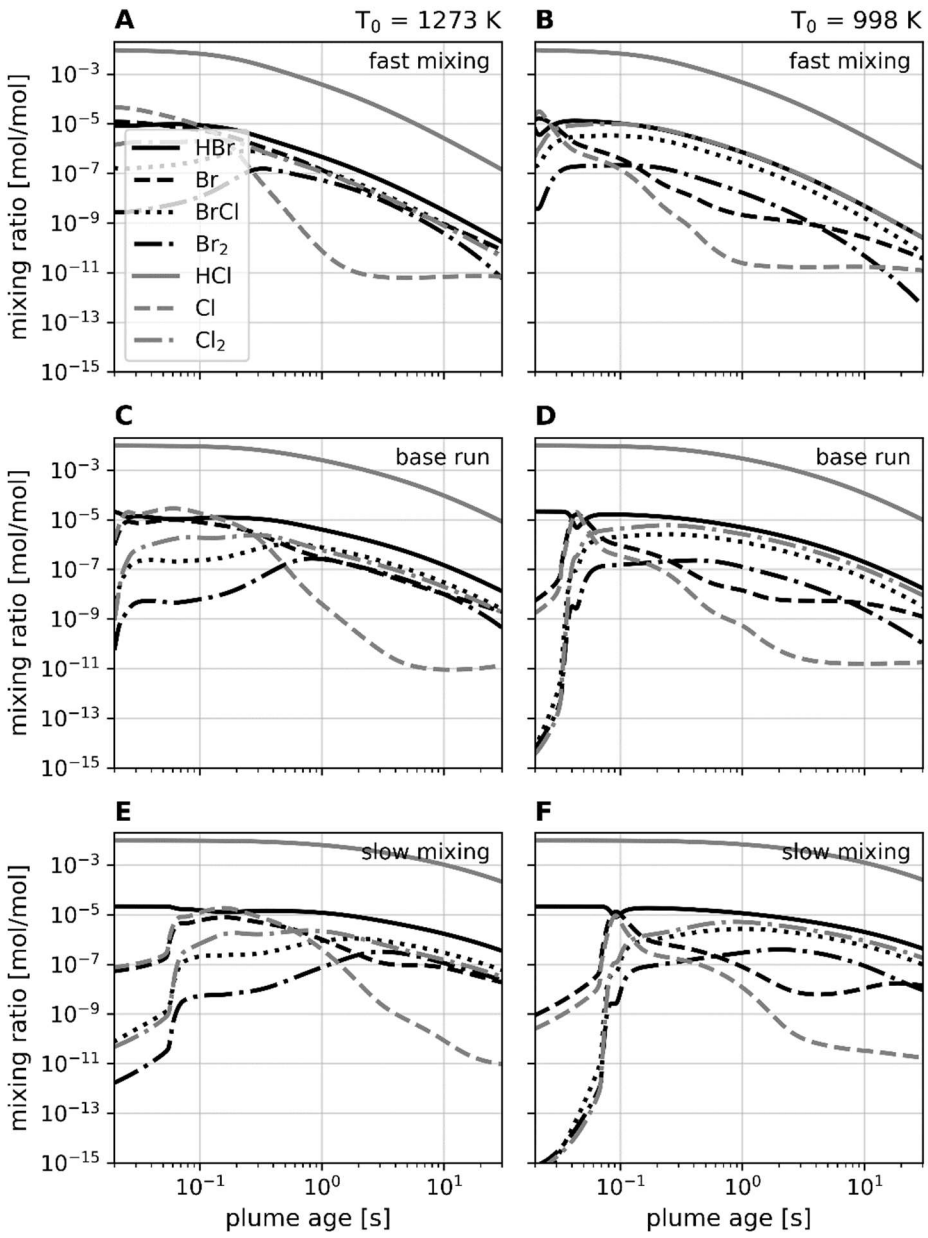

Figure S 8: Halogen speciation for the Redoubt plume case study for two emissions temperatures (T_0 = 1273 K, 998 K) and three mixing scenarios. Shown are the dominant reactive halogen species involved in the oxidation of Hg and the primary emitted hydrogen halides HBr and HCl.

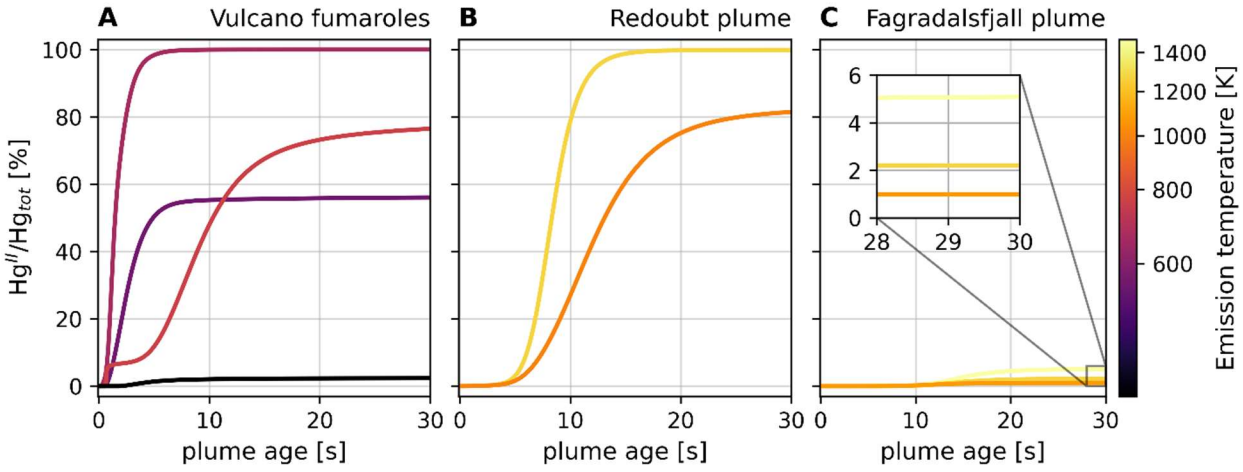

Figure S 9: Model results of the emission temperature sensitivity study for the slow mixing scenario. Percentage of total mercury in the form Hg^{II} simulated over 30 s for halogen-rich Vulcano, Mt Redoubt and halogen-poor Fagradalsfjall plumes.

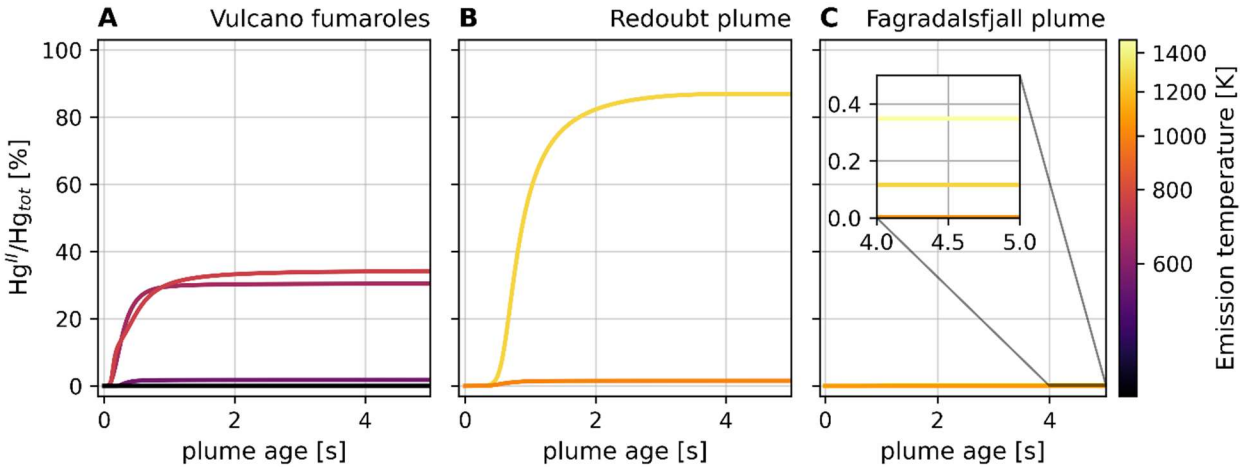

Figure S 10 Model results of the emission temperature sensitivity study for the fast-mixing scenario. Percentage of total mercury in the form Hg^{II} simulated over 5 s for halogen-rich Vulcano, Mt Redoubt and halogen-poor Fagradalsfjall plumes.

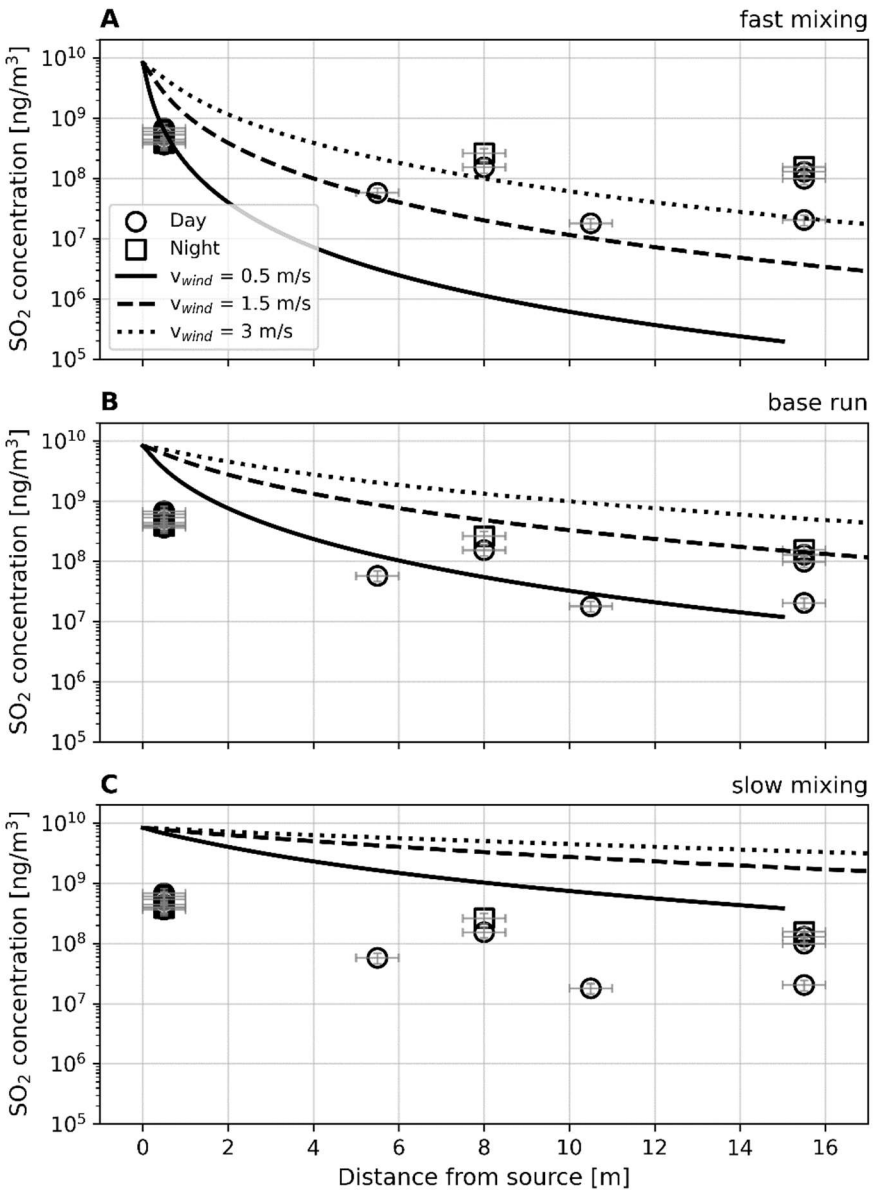

Figure S 11: Distance resolved SO_2 measurements at Vulcano fumaroles (black markers) and model SO_2 dilution (black lines) for the three mixing scenarios. The line style indicates different windspeeds or plume transport speeds between 0.5, 1.5 and 3 m/s (estimated range based on hand-held anemometer).

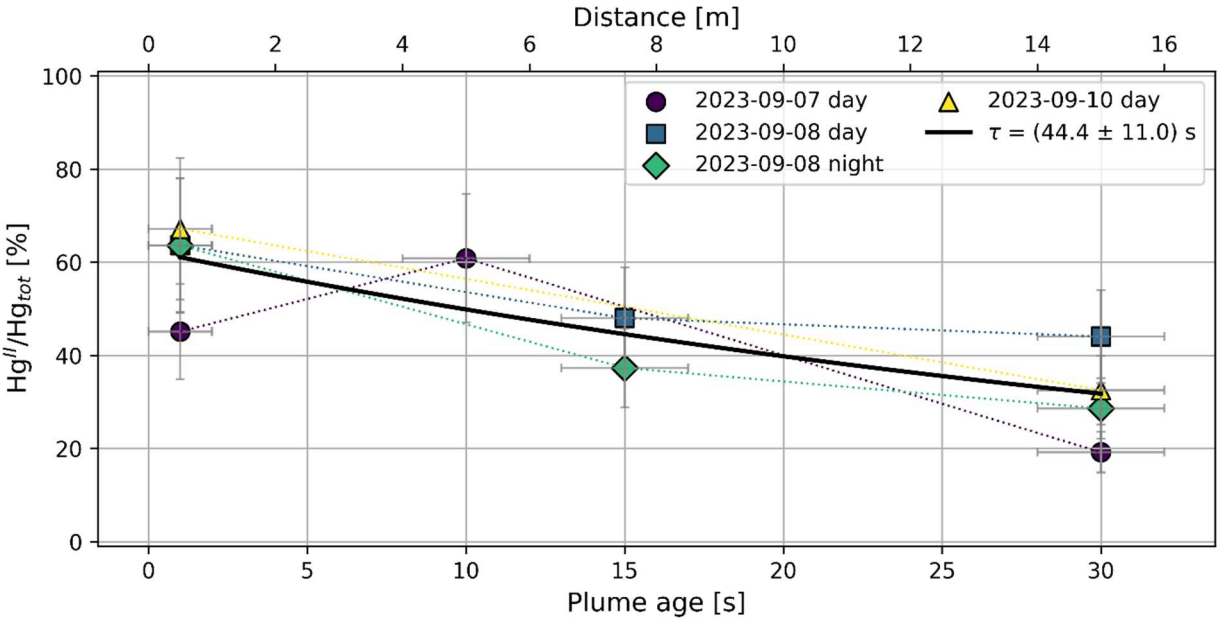

Figure S 12: Hg^{II}/Hg_{tot} ratio in % plotted as a function of plume age (distance on second x-axis). Different markers correspond to different measurement days. Measurements are performed simultaneously at different distances from the emission source and plume age is calculated according to a windspeed of 0.5 m/s. Error-bars are given based on uncertainty estimations of the distance determination. The black and corresponds to an exponential decay fit with a lifetime of Hg^{II} of (44.4 ± 11.0) s.

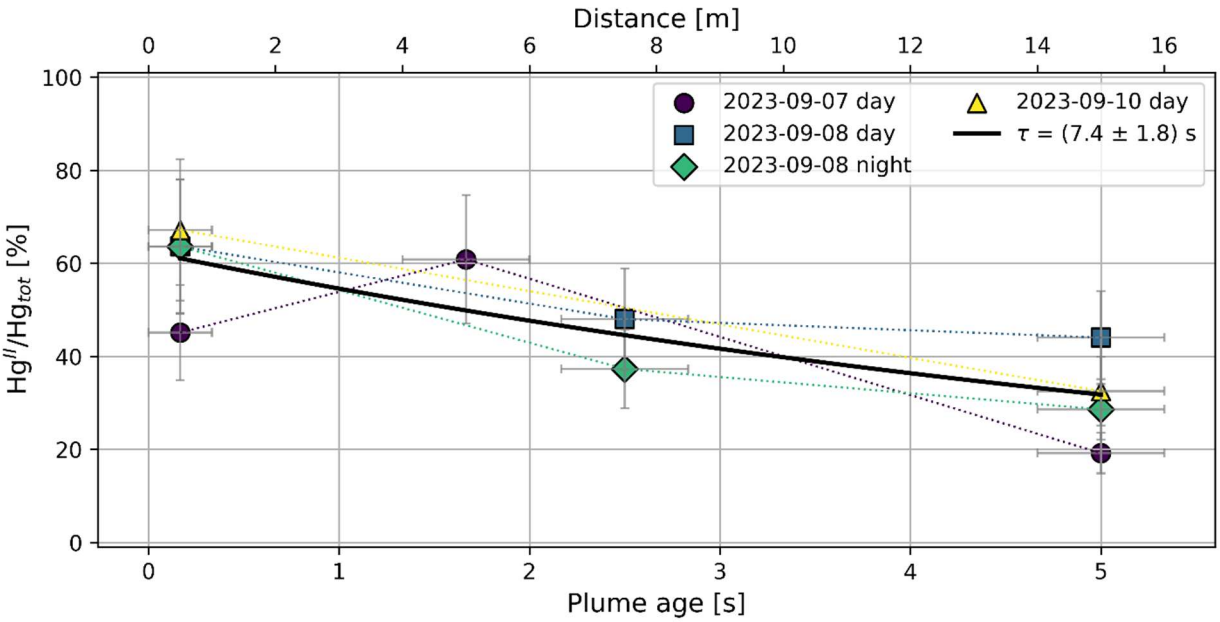

Figure S 13: Hg^{II}/Hg_{tot} ratio in % plotted as a function of plume age (distance on second x-axis). Different markers correspond to different measurement days. Measurements are performed simultaneously at different distances from the emission source and plume age is calculated according to a windspeed of 3 m/s. Error-bars are given based on uncertainty estimations of the distance determination. The black line corresponds to an exponential decay fit with a lifetime of Hg^{II} of (7.4 ± 1.8) s.

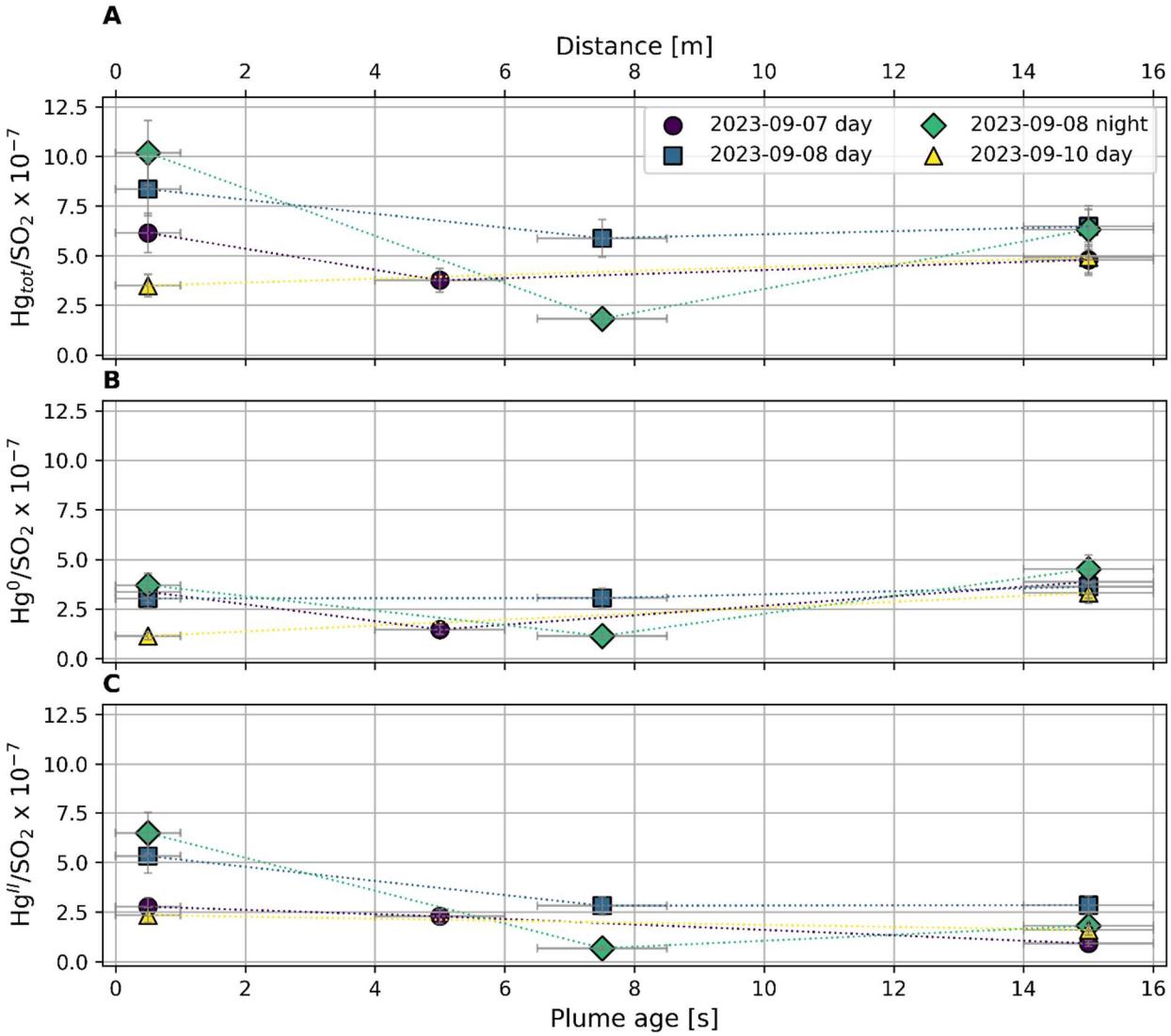

Figure S 14: Comparison of the Hg_{tot}/SO_2 (Panel A), Hg^0/SO_2 (Panel B), and Hg^{II}/SO_2 (Panel C) ratios for the four distance resolved measurements at fumarole F0.